Chapter 2

BINDING ASYMMETRY IN TELECHELIC POLYMER NETWORKS

2.1 Abstract

Networks assembled by the reversible self-association of telechelic polymers are a common class of soft materials. Here we show that, within any such network, the sequential binding of identical chain ends to the network is inherently asymmetric: the first association is always stronger than the second. This binding asymmetry primarily arises from a strong entropic penalty for chain entry into the fully bound state due to local network structure. We derive a simple equation predicting the degree of binding asymmetry as a function of network geometry from equilibrium statistical mechanics. A large set of self-diffusivity measurements on a series of model telechelic polymers finds good agreement with this new theory. Generalized binding asymmetry for chains with many associative domains also holds.

2.2 Introduction

Entropic constraints underlie the structure and dynamics of macromolecular systems. For example, decreased entropy associated with chain stretching is the basis for the elasticity of polymer networks (*1*). Negative entropies of mixing can promote phase separation of polymer solutions at elevated temperatures (*2, 3*). Entropy also regulates many aspects of protein function, including allostery, ligand recognition, and catalytic activity (*4-9*). Here we describe a new binding phenomenon in reversible polymer networks that is under entropic control.

Reversible polymer networks are a well-studied class of materials, and consist of polymers crosslinked through non-covalent or physical means (e.g., by hydrogen bonding or chain entanglement) (*10-13*). Telechelic polymers can spontaneously assemble such networks via reversible self-association of their reactive end-groups (*14-21*). The end-groups cluster into discrete junctions that act as transient interchain crosslinks. Stress relaxation within the resulting network structure is mediated by chain disengagement from the junctions. Importantly, the same event can also permit diffusion of disengaged chains throughout the network (*21*). Relating the bulk material properties of reversible networks to the single chain picture has been the goal of several important theoretical treatments (*22-24*).

Towards the same goal, we model telechelic networks as an ensemble of chains partitioned into three sequential states, depicted schematically in **Figure 2.1A**. In the free state *f*, neither chain end is bound to the network. By reversible association with the network, the chain may transition into either the dangle state *d* (one end bound) or the bound state *b* (both ends bound). Two different topologies are possible in the bound state: bridges (*B*) and loops (*L*). Conversion among the three states is controlled by the equilibrium constants $K_1 = [d]/[f]$ and $K_2 = [b]/[d]$. Since $[b] = [B] + [L]$ we may also write K_2 as the sum of bridges and loops, i.e. $K_2 = [B]/[d] + [L]/[d] = K_B + K_L$. Given that the two ends of a telechelic polymer are structurally identical, one might naively expect symmetry between these two constants, i.e. $K_1 = K_2$. We will now demonstrate both theoretically and experimentally that this is essentially never true. Binding asymmetry, with $K_1 > K_2$, will

always arise in this simple system due to purely entropic considerations, regardless of the binding energy or the detailed crosslinking mechanism.

2.3 Theory

2.3.1 Statistical mechanics of telechelic chain binding

Consider a single telechelic chain undergoing reversible network association (**Figure 2.1A**). The ideal chemical potential for the chain in the free state (neglecting interchain interactions) may be taken as $\beta\mu_f = \ln(n_c[f]\upsilon_{ref}) - \ln(G_f)$, where $\beta = 1/k_BT$, n_c denotes the number density of chains, and υ_{ref} is a reference volume. The conformational entropy of the free chain is contained within $G_f = G_f(\mathbf{R}; N, b)$. We treat the unbound chain ends as distinguishable such that $G_f = \int p(\mathbf{R}; N, b) d\mathbf{R}$, where $p(\mathbf{R}; N, b)$ is the vector end-to-end distance probability density function.

Upon binding once (transition from free to dangle), the chain energy changes by an amount ΔE_B, and the chain also becomes restricted to a small fraction of the total system volume $\phi_j \equiv \upsilon_j n_j$, where υ_j is the local volume accessible to a dangling chain and n_j is the junction number density. Although translational entropy is lost upon tethering one chain end, we assume no additional loss of conformational freedom, since the untethered end is still free to explore space around the junction itself, the size of which is relatively small. These considerations provide $G_d \approx 2G_f$, where the factor of 2 arises because a dangling chain has two ends available for binding the network. The chemical potential of a dangling

chain is then $\beta\mu_d = \ln(n_c[d]\upsilon_{ref} / \phi_j) - \ln(2G_f) + \beta\Delta E_B$, and from the equilibrium condition ($\mu_f = \mu_d$) we obtain $K_1 = 2\phi_j \exp[-\beta\Delta E_B]$.

The chain faces a new challenge during the second binding event (transition from dangle to bound). In order to adopt the bridge topology *B*, the second chain end must locate a new junction within a restricted volume fraction $\phi_j(\mathbf{R}; R_{mesh})$ some distance $\mathbf{R}$ away from the first chain end. This volume necessarily depends on the local network structure, with $\phi_j(\mathbf{R}) = \phi_j g(\mathbf{R})$, where $g(\mathbf{R})$ is the pairwise junction density distribution function. If the preferred size of the free or dangling chain is small relative to R_{mesh}, the characteristic mesh size (junction spacing) of the network, significant conformational entropy may be lost during bridge formation. The chain may prefer to adopt the loop topology *L* if the junction spacing is sufficiently wide.

To account for these possibilities, we treat the chemical potential of a bound chain as a sum of bridges and loops, with the bridge configurational integral weighted by the local junction density. We define $\phi_j G_b \equiv \phi_j G_B + G_L$, where $\phi_j G_B = \phi_j \int p(\mathbf{R}) g(\mathbf{R}) d\mathbf{R}$ is the conformational entropy of bridged chains. G_L for loops takes the same functional form as G_f and G_d, but we restrict the bounds of the conformational integral to a small distance *l* on the order of the junction size (end-to-end distance of looped chains), rather than the junction spacing. The bound chain chemical potential is then $\beta\mu_b = \ln(n_c[b]\upsilon_{ref} / \phi_j^2) - \ln(G_b) + 2\beta\Delta E_B$, and we obtain K_2 from the equilibrium condition ($\mu_d = \mu_b$) as $K_2 = \exp[-\beta\Delta E_B](\phi_j G_B + G_L) / 2G_f$.

This analysis results in the following expression for the ratio of K_1 to K_2 for a telechelic polymer:

$$\frac{K_1}{K_2} = \frac{4G_f}{G_B + G_L/\phi_j} \qquad \textbf{(Eq. 1)}$$

The ratio is independent of the binding energy. If we neglect loops entirely and consider only bridges ($G_L = 0$), the ratio is simply:

$$\frac{K_1}{K_2} = \frac{4G_f}{G_B} = \frac{4\int p(\mathbf{R})d\mathbf{R}}{\int p(\mathbf{R})g(\mathbf{R})d\mathbf{R}} = \frac{K_1}{K_B} \qquad \textbf{(Eq. 2)}$$

Eq. 2 distills our key prediction for the reversible binding of telechelic polymers: K_1 and K_2 will be inequivalent in any network containing a significant fraction of bridges. More specifically, apart from a complete absence of network structure (i.e., junctions are randomly distributed in space such that $g(\mathbf{R}) = 1$), we will always have $K_1 \geq 4K_2$. This asymmetry arises as a natural consequence of network formation, which can reduce the set of conformations available to bridged chains due to the local depletion of junctions on length scales relevant to the free and dangling chains. Moreover, in addition to this structural asymmetry, the first association is inherently four times stronger than the second, since the dangling state always has twice as many ways to bind the network as either the free or the bound states.

We can estimate the strength of these entropic effects directly from **Eq. 2**. Assume "probe" chains with $N = 100$ monomers each of unit length $b = 1$ are partitioned in a "normal

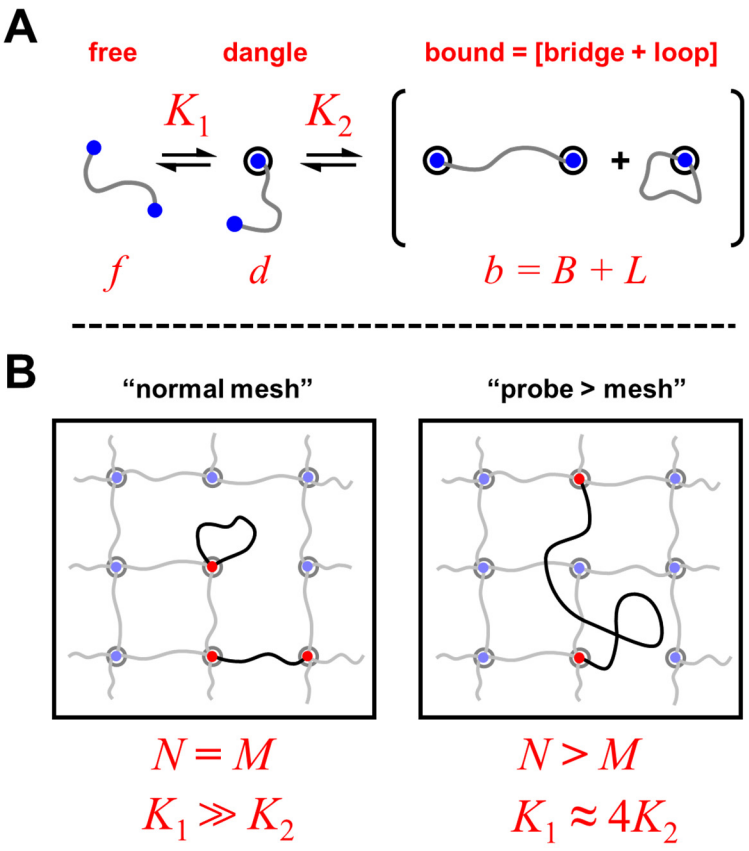

Figure 2.1. Schematic representation of single chain partitioning in a reversible telechelic network. (**A**) The chains are partitioned among three sequential states: free (*f*), dangle (*d*), and bound (*b*). The bound state consists of bridges (*B*) and loops (*L*). (**B**) Predicted dependence of binding asymmetry (K_1 / K_2) on the mesh size (*M*) and probe size (*N*). Strong asymmetry is expected for the size-matched "normal mesh". Reduced asymmetry is expected for the case where the probe is much larger than the mesh.

mesh" made from chains having the same size $M = 100$ (**Figure 2.1B**). For simplicity, we take $p(\mathbf{R}; N, b) = (3/2\pi Nb^2)^{3/2} \exp(-3\mathbf{R}^2 / 2Nb^2)$ for a Gaussian chain (*25*) and model $g(\mathbf{R}; R_{mesh})$ as a step function activated at a characteristic mesh size $R_{mesh} = 10$. The

characteristic dimensions of the probe are $R_{probe} = bN^{1/2}$, such that $r \equiv R_{probe} / R_{mesh} = 1$. Integrating over the probe chain from $R = 0$ to $R_{max} = Nb$ gives $K_1 / K_2 = 10.21$. Increasing the size of the probe while keeping the network dimensions fixed (**Figure 2.1B**, "probe > mesh") should reduce the degree of asymmetry, since the test chain is less conformationally constrained upon entering the bridge state. Indeed, using $N = 500$ in the above calculation provides $K_1 / K_2 = 4.46$. For an infinitely long probe in a finite mesh, **Eq. 2** predicts that the binding asymmetry arising from network structure will disappear completely ($K_1 / K_2 = 4$). In this case the untethered chain end behaves like a free chain end: it has a global "view" of the network (it can access all available sites) such that bridge formation is not constrained by the other end. In any real network, the above effects will depend on concentration through loops, which we propose to capture with **Eq. 1**.

2.3.2 Generalization to chains with multiple stickers

The above, intuitive derivation of binding constants for telechelic chains may be generalized for chains with multiple associative domains ("stickers") along the backbone using a more formal approach. In general, for a multisticker probe with *S* such stickers, one can define an equilibrium constant K_i as the ratio of the number of chains with i to $i-1$ bound chains. One then readily finds

$$K_i = \frac{Z_i}{Z_{i-1}} \exp(-\beta \Delta E_B) \qquad \textbf{(Eq. 3)}$$

where Z_i is the sum of all possible chain configurations with *i* bound stickers, subject to the constraint of chain connectivity. For a chain with *S* total stickers, the number of ways

N_b in which $i \leq S$ such stickers may become bound is simply the binomial coefficient $N_b = C(S,i)$. We can then express $Z_i = \sum_{k=1}^{N_b} Q_k$, where Q_k is the sum of all configurations available to a chain in the k^{th} bound state (**Supplementary Figure 2.1**). The chain can be thought to consist of $S - 1$ flexible "blocks" between each sticker. The total number of configurations available to the whole chain in the k^{th} bound state can be decomposed into the product of the configurations available to each $S - 1$ block, such that $Q_k = \prod_{j=1}^{S-1} G_{k,j}$. The central task is then to compute the number of configurations available to each block for a given bound state of the chain. We derive the exact results for the cases of $S = 3$ and $S = 5$ in the **Supporting Information** (**Supplementary Table 2.1**). Our key prediction for multisticker chains is that $K_i \ll K_{i-1}$ for all sequential associations.

2.4 Results and Discussion

2.4.1 Network design and characterization

We designed a series of model, reversible telechelic networks to test these predictions. Artificial proteins are well suited to exploring the physical properties of reversible networks: they are structurally well-defined, completely monodisperse, and are easily modified (e.g. chain extended) by manipulating their DNA coding sequences. We cloned and recombinantly expressed a large family of P(E$_n$P)$_m$-type protein polymers (**Supplementary Figure 2.2**), where P is an associative domain that forms pentameric coiled-coils (network junctions), and E$_n$ is a flexible elastin-like linker (**Supplementary Tables 2.2** and **2.3**). When swollen in aqueous buffer, PE$_n$P proteins formed completely transparent hydrogels with classical Maxwell-type rheological signatures (**Supplementary**

Figures 2.3 and **2.4**). We could easily vary the mesh size and terminal modulus of each gel by changing the number of repeats of the elastin midblock (n = 3 – 24), without perturbing the network relaxation rate (**Supplementary Figure 2.5** and **Supplementary Table 2.4**). The terminal network moduli of each "n-mesh" approximated the molecular weight dependence expected from rubber elasticity theory ($G'_\infty \sim M^\nu$), with $\nu = -1$ expected for simple affine networks (*25*), and $\nu = -0.9 \pm 0.2$ observed experimentally (**Supplementary Figure 2.5**).

2.4.2 Measurement of equilibrium constants

The equilibrium constants K_1 and K_2 for telechelic polymers were estimated in each n-mesh by inferring them from effective diffusivities of size-matched ($N = M$) and mismatched ($N \neq M$) fluorescently-labeled test chains ("n-probes", n = 3 – 48) with either zero (E_n^*), one (E_nP^*), or two (PE_nP^*) terminal coils (**Figure 2.2A**). The effective diffusivity D_S of a test chain with S associative domains can be related to each S^{th}-order equilibrium constant using:

$$\frac{D_0}{D_S} = 1 + K_1 + K_1K_2 + \cdots + \prod_{i=1}^{S} K_i = 1 + \sum_{j=1}^{S}\left(\prod_{i=1}^{j} K_i\right) \qquad \textbf{(Eq. 4)}$$

where $D_0 = D_f$ is the diffusivity of chains in the free state (*21*). We first measure D_0 by monitoring the fluorescence recovery rate of an E_n^* test chain that cannot bind to the network and is therefore locked in the free state. The diffusivity is obtained by fitting the FRAP trace to a renormalized Fickian diffusion model (see **Materials and Methods**) (*21, 26, 27*). Next, K_1 is obtained from **Eq. 4** by comparing the mobility D_1 of an E_nP^* probe

with D_0. This comparison provides a direct estimate for the key exponential factor $K_{1/2} = \phi_j \exp[-\beta \Delta E_B]$, the equilibrium constant for non-telechelic chains with only one sticker. $K_1 = 2K_{1/2}$ for telechelic chains is then easily obtained. Subsequently, K_2 for telechelic chains is obtained by comparing the mobility D_2 of a PE_nP^* probe with D_0, and supplying the measured value of K_1 into **Eq. 4**. At each step we adjust D_0 slightly by the Rouse scaling $D_0 \sim 1/N$, to take into account the added mass of each P domain. An important assumption implicit in the derivation of **Eq. 4** is that network chains have a negligible mobility once bound to the network, such that all chain migration occurs through a "hopping" mechanism. In this mechanism, single chains must completely disengage from the network (enter the free state) in order to travel distances greater than $\sim O(R_{mesh})$ (*21*). We examine this assumption further below.

We acquired a total of 298 FRAP traces on 15 different probes in four different meshes in order to explore a wide range of different R_{probe} / R_{mesh} ratios. Since the bleach spot profile was found to be moderately sensitive to the nature and size of the probe (**Supplementary Figure 2.6**, we acquired an additional 173 control FRAP traces on size-matched E_n^* probes in each of the four meshes (**Supplementary Figure 2.7**). Using a generalized Gaussian bleach spot fit-and-track algorithm, our inferred diffusivities were insensitive to the variance in the bleach spot profile over a wide range of bleach efficiencies. Representative FRAP traces for each of the probes in the 6-mesh network, along with their corresponding Fickian diffusion fits, are presented in **Supplementary Figure 2.8**. Each D_S obtained from

all 15×4 combinations of probes and meshes ($n \geq 4$ replicates per combination) is plotted separately in **Supplementary Figure 2.9**.

2.4.3 Power-law fits to diffusivity data

Power-law fits to the diffusivity dataset, with $D_S \sim N^{\alpha_s}$, provide molecular weight exponents α_s that permit estimation of β_i for each $K_i \sim N^{\beta_i}$ (**Supplementary Figure 2.9** and **Supplementary Table 2.4**). These estimates are qualitatively consistent with **Eq. 1** and **Eq. 2**. In the 6-mesh, for example, $\alpha_0 = \text{-}1.5 \pm 0.0$, $\alpha_1 = \text{-}0.9 \pm 0.1$, and $\alpha_2 = \text{-}1.5 \pm 0.1$ for D_0, D_1 and D_2 respectively (**Figure 2.2B**). A scaling analysis of **Eq. 4** provides $\beta_1 = \alpha_0 - \alpha_1 = \text{-}0.6 \pm 0.1$ for K_1, and $\beta_2 = \alpha_1 - \alpha_2 = 0.6 \pm 0.1$ for K_2. The molecular weight exponent for K_2 is positive, implying increasing association strength of the second chain end as the chain becomes longer. $K_1 / K_2 = \beta_1 - \beta_2 = \text{-}1.2 \pm 0.1$ is strongly negative, consistent with weakening of the structural asymmetry as the entropic constraint for bridge entry is relaxed. We attribute the negative value of β_1 to excluded volume effects (e.g., end group association starts to become sterically hindered by the large pervaded volume of the chain itself), which are not captured by our theory. We presume that such effects would hinder both associations equally, in which case they should be approximately absent from the experimental K_1 / K_2 ratio.

2.4.4 Coarse-graining of *n*-probes as equivalent freely jointed chains

A quantitative comparison of the dataset to **Eq. 1** and **Eq. 2** requires an estimate of R_{mesh} for each mesh, and coarse-grained estimates of R_{probe} for each probe in terms of b and N,

the Kuhn length and number of monomers for an equivalent freely jointed chain. For this purpose, we select the Flory characteristic ratio $C_\infty = 2.51$, calculated for elastin pentapeptides using conformational energy maps (*28*). Although recent DLS measurements on model elastins in water provide slightly larger ratios (*29, 30*), $C_\infty = 2-3$ is typical for denatured glycine-rich proteins in a θ-solvent (*31, 32*). Moreover, measurements of the second virial coefficient for model elastins suggest a θ-temperature between 40 and 45 °C (*30*), justifying our treatment of the chains as essentially ideal.

For an ideal chain, $R_{probe} = (C_\infty n_p l_p{}^2)^{1/2} = bN^{1/2}$ and $R_{max} = n_p l_p$, where we take n_p to be the number of peptides between each associative domain, and $l_p = 0.38\,\text{nm}$ is the approximate linear C_α–C_α distance (*32*). We assign the length of a Kuhn monomer as $b = C_\infty n_p l_p{}^2 / R_{max} = 0.95$ nm (*25*). The equivalent freely jointed chain is then composed of $N = R_{max}{}^2 / C_\infty n_p l_p{}^2$ such monomers, each with an effective molar mass of $M_0 = 198$ Da. Between our smallest (3-probe) and largest (48-probe) chains, R_{probe}= 6.14 – 21.36 nm, and N varies from 41 to 502 respectively. These data are summarized in **Supplementary Table 2.5**. We select R_{mesh} based on the junction number density n_j, which provides $R_{mesh} = 12.15 - 17.32$ nm between the 3-mesh and 24-mesh at a fixed mass concentration of $\rho = 100$ g/ L. Under these conditions, $r \sim bN^{1/2}M^{-1/3}$ such that binding asymmetry is expected to decrease with increasing molecular weight in size-matched networks (i.e., if $N = M$ and the chain is ideal, $r \sim bM^{1/6}$).

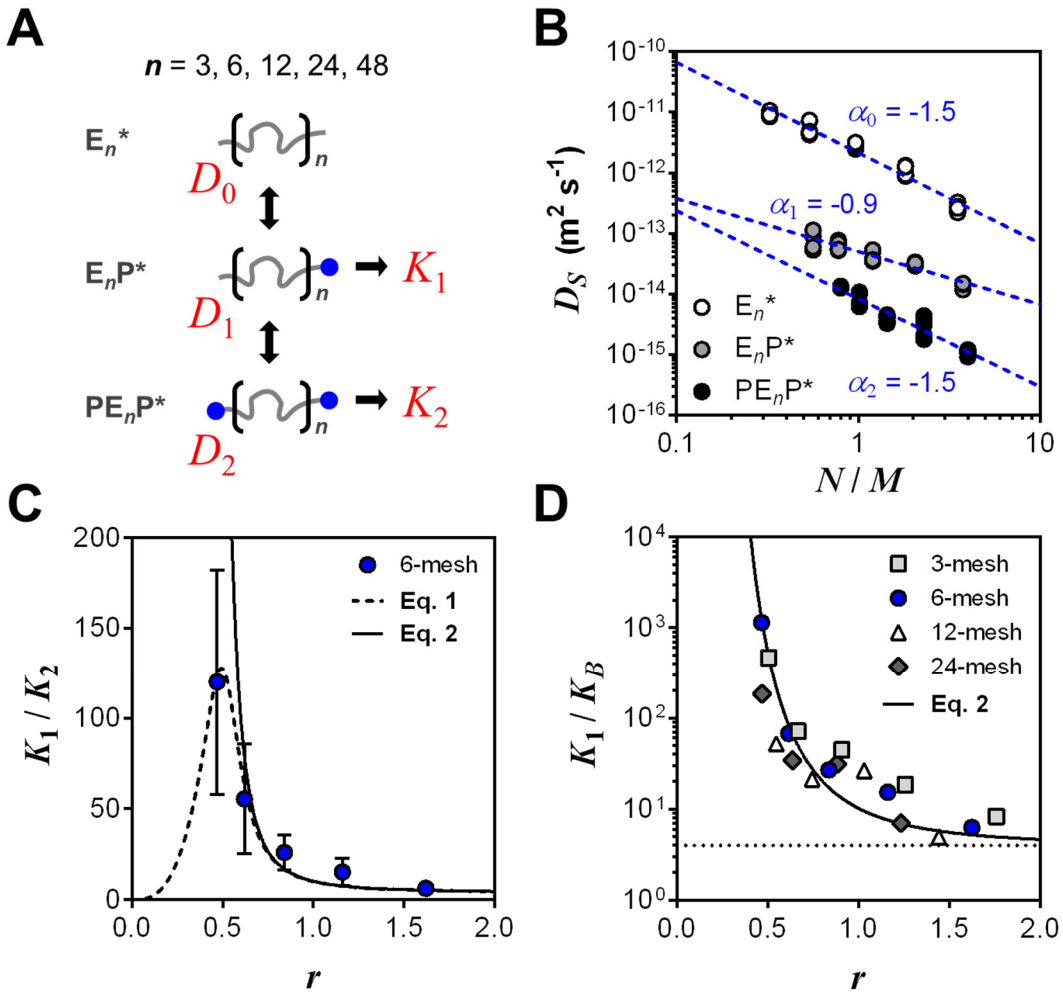

Figure 2.2. Binding asymmetry in telechelic polymer networks. (**A**) Elastin-like probes with different lengths and numbers of stickers were placed in size-matched ($N = M$) and mismatched ($N \neq M$) PE$_n$P "n-mesh" networks. Equilibrium constants were inferred from diffusivities extracted by FRAP (**Eq. 4**). (**B**) Representative diffusivities in a 6-mesh ($n = 80$ measurements, ≥ 4 per probe). Molecular weight exponents α_i for each D_S were extracted from power-law fits. (**C**) Experimental K_1 / K_2 data (mean ± std. dev.) in the 6-mesh plotted against $r = R_{probe} / R_{mesh} \sim bN^{1/2}M^{-1/3}$. Predictions from **Eq. 1** and **Eq. 2** are shown, with $x_{min} = 0.26$. (**D**) Loop subtraction permits a simultaneous comparison of the K_1 / K_B data from each mesh ($n = 271$ total measurements) to **Eq. 2** using $x_{min} = 0.24 – 0.43$. Error bars are omitted for clarity. The dotted line represents $K_1 / K_B = 4$.

2.4.5 Quantitative comparison to theory

A functional analysis of **Eq. 2** reveals that K_1 / K_2 is completely specified by the dimensionless probe size *r*, whereas **Eq. 1** contains an effective *N* dependence through $\phi_j = n_j \upsilon_j$ and the looping integral G_L. We account for this by modeling the accessible volume of junction-bound chains as $\upsilon_j = 4\pi c^3 / 3$, where *c* is the characteristic dimension of a cluster. Estimates based on the molecular weight of the P domain provide *c* = 1.89 nm (**Supplementary Equations and Derivations**). The *N* dependence may then be captured through *l*, the limits of the looping integral. At fixed $x \equiv l / c$ ratios, the behavior of **Eq. 1** is nearly independent of *c* for $c < R_{mesh}$ due to the approximate cubic form of the volume integral $G_L \sim l^3$, and the fact that $\phi_j \sim c^3$ (**Supplementary Figure 2.10**). We expect $l \sim O(b)$, and indeed, selecting *l* based on rheological data provides *l* = 0.29 – 1.52 nm. In practice we choose $l = l_{min}$ to minimize the residuals between **Eq. 1** and the experimental values in each mesh (**Supplementary Figure 2.11**).

Experimental values of K_1 / K_2 in the 6-mesh are plotted against *r* in **Figure 2.2C**, along with the theoretical predictions of **Eq. 1** and **Eq. 2**. The data are in good agreement with the theory: K_1 / K_2 rises sharply for *r* < 1, and decays for *r* > 1. The experimental rise in K_1 / K_2 appears softened by loop formation at low *r*, an effect that is more significant in the larger meshes (**Supplementary Figure 2.12**). To compare the data in all meshes simultaneously, we subtract out the estimated looping contributions from the experimental data using $K_1 / K_B = [(K_2 / K_1)_{exp} - G_L / 4\phi_j]^{-1}$. Selecting x_{min} = 0.24 – 0.43 to minimize the looping residuals in each mesh leads to a satisfying collapse of the dataset onto **Eq. 2**

(**Figure 2.2D**). $G_L / 4\phi_j > (K_2 / K_1)_{exp}$ for two of the 20 R_{probe} / R_{mesh} ratios (loops are slightly overestimated), which we exclude from the master plot. This can be avoided by choosing a smaller x_{min} = 0.26 for all meshes (fit to the 6-mesh), and a fit of comparable quality is still achieved (**Supplementary Figure 2.13)**. Experimentally, K_1 / K_B varies over a remarkable 200-fold range and exceeds 10^3 for r = 0.47, the smallest probe in a 6-mesh. This demonstrates the strong entropic penalty paid by chain entry into the bridge state. Moreover, the data appear to asymptote at $K_1 / K_2 = 4$: $K_1 / K_B = 4.94 - 8.27$ is obtained over r = 1.23 – 1.76, the ratios for the largest probes in each mesh.

To directly test the concentration dependence of **Eq. 1**, we acquired an additional 54 FRAP traces in size-matched 6-mesh networks at four additional mass concentrations ($\rho = 50 - 250$ g/ L), with $\phi_j \sim (c / R_{mesh})^3$ = 0.012 – 0.057. These data are plotted in **Figure 2.3** against **Eq. 1** with x_{min} = 0.37 ± 0.05. Strong formation of loops is evident experimentally at the lowest concentrations, with $K_1 / K_2 \sim \phi_j$ for small ϕ_j. K_1 / K_2 then falls sharply above $\phi_j = 0.035$, consistent with increased bridge formation as the junction spacing becomes smaller. Both of these effects are captured by **Eq. 1**, although the experimental drop in K_1 / K_2 is sharper than the theory predicts due to a predicted rise in K_2 that is too slow (**Supplementary Figure 2.14**). Excluded volume effects in the real network may be important at these higher concentrations, and cooperative self-assembly of the P domain cannot be excluded. It is interesting to note that **Eq. 1** specifies a region at very low $\phi_j < \phi_j^* = G_L / (4 - G_B)$, for which $K_1 < K_2$ and the binding asymmetry inverts. This region appears physically implausible, since it lies below the mean-field percolation

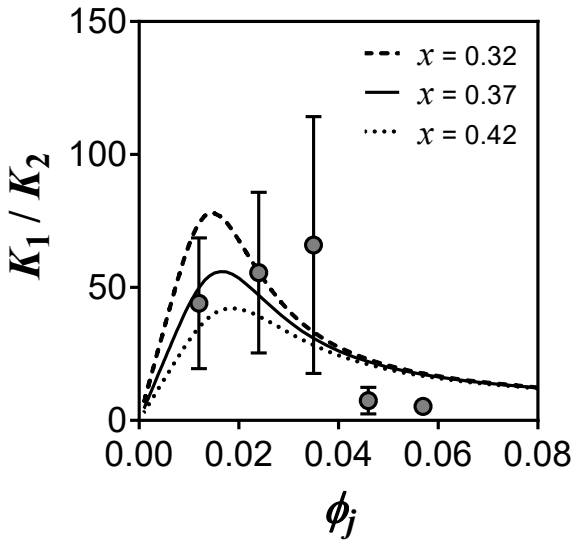

Figure 2.3. Dependence of K_1/K_2 on junction density. Binding asymmetry is proportional to ϕ_j for small $\phi_j \sim R_{mesh}^{-1/3}$, then falls sharply above $\phi_j \sim 0.035$ due to a decrease in interjunction spacing. **Eq. 1** qualitatively captures this behavior, with $x_{min} = 0.37 \pm 0.05$. The data were collected in a 6-mesh network, and predictions from **Eq. 1** were generated using coarse-grained data on 6-mesh probes, with $b = 0.95$ and $N = 72$ (**Supplementary Table 2.3**). Error bars depict mean ± std. deviation from n = 76 total measurements, with ≥ 2 measurements per probe per concentration. The mass concentration of each network ranged from 5 – 25% (*w*/*v*), i.e. ρ = 50 – 250 g/L.

threshold for an *f*-functional Bethe-lattice, $p_c = 1/(f-1) = 1/4$ for $f = 5$. Substituting ϕ_j^* into **Eq. S15**, provides the theoretical maximum bridge fraction $[B]^* = G_B/4 \leq p_c$ for all *N*. Hence we always expect $K_1 > K_2$, at least for networks assembled from pentameric crosslinking domains.

Generalization of our theory to chains having $S > 2$ stickers using **Eq. 3** suggests that the entropic penalty for entry into the bridge state becomes compounded with each sequential

association, such that $K_i < K_{i-1}$ for all $i \leq S$ (**Supplementary Table 2.1**). Intuitively, we expect each sequential association to become more costly as the conformational restriction on the whole chain grows. This is expected to greatly increase the fraction of free chains, and thus the likelihood that a chain will migrate by "hopping" (complete site disengagement before rebinding). To test this hypothesis, we synthesized two additional "multisticker" probes, with S = 3 and S = 5, and compared their effective diffusivities, measured in a 6-mesh network, to the exact theoretical predictions for blocks of this size, obtained from **Eq. 3**.

To permit a direct comparison, we define the effective equilibrium constant $K_{eff} = \left[\sum_{j=1}^{S} \left(\prod_{i=1}^{j} K_i \right) \right]^{1/S}$, such that $D_0 / D_S = 1 + K_{eff}{}^S$ from **Eq. 4**. Moreover, we calculate $D_{hop} = p_f D_0$, where p_f is the fraction of free chains computed from **Eq. 3**. To ensure a correct estimation of the looping fraction, we select x_{min} = 0.37 based on minimization of residuals in the 6-mesh concentration series. We observe striking agreement between the generalized asymmetric binding theory and our measured values of K_{eff} for both S = 3 and S = 5 (**Figure 2.4**). The D_{hop} prediction is essentially exact for S = 3, and D_{hop} / D_S = 0.33 for S = 5, i.e. ca. 33% of these multisticker chains still migrate by hopping, despite the large number of stickers. These predictions hold over several different reasonable estimates of ϕ_j and x. We note that the measured D_S for S = 5 approaches a theoretical bound mobility $D_b = R_{mesh}{}^2 / 6\tau_b = 1.61 \times 10^{-17}$ m^2 s^{-1}, where we have assumed that a bound chain can move a distance of order the mesh size within a bound time $\tau_b \sim \omega_c{}^{-1} \approx 1$ s set by the

relaxation rate of the network (**Supplementary Figure 2.5**). Thus we suspect that, for S = 5, the motion of the remaining chains is slaved to the collective reorganization of the telechelic network itself, in agreement with recent work by Tang et al. (*33*). Notably, ignoring the asymmetry in the binding constants drastically understimates the fraction of free chains. Moreover, a prediction from Baxandall that multisticker self-diffusion should be Rouse-like, with $D_S \sim 1/S$, appears too weak (*23*).

2.5 Conclusion

Our results support a new theory of asymmetric binding in reversible networks of telechelic polymers. For telechelic chains, the first association is always greater than the second due to a strong entropic constraint on entry into the bridge state. This constraint arises from a local depletion of network junctions on length scales preferred by the dangling chain. The chain must therefore discard a rich set of conformations in order to effectively bridge network junctions, whereas this constraint is essentially absent during the first association. This leads to $K_1 \gg K_2$ for most networks, and for size-matched networks, the asymmetry is especially strong at low N. The effect is compounded for chains with multiple associative domains, leading to $K_{i-1} \gg K_i$ in general, promoting diffusive chain transport that remains strongly influenced by hopping, even for chains with up to five associative domains.

2.6 Acknowledgements

The technical assistance of Andres Collazo at the Caltech Beckman Imaging Center during the acquisition of the FRAP data is gratefully acknowledged.

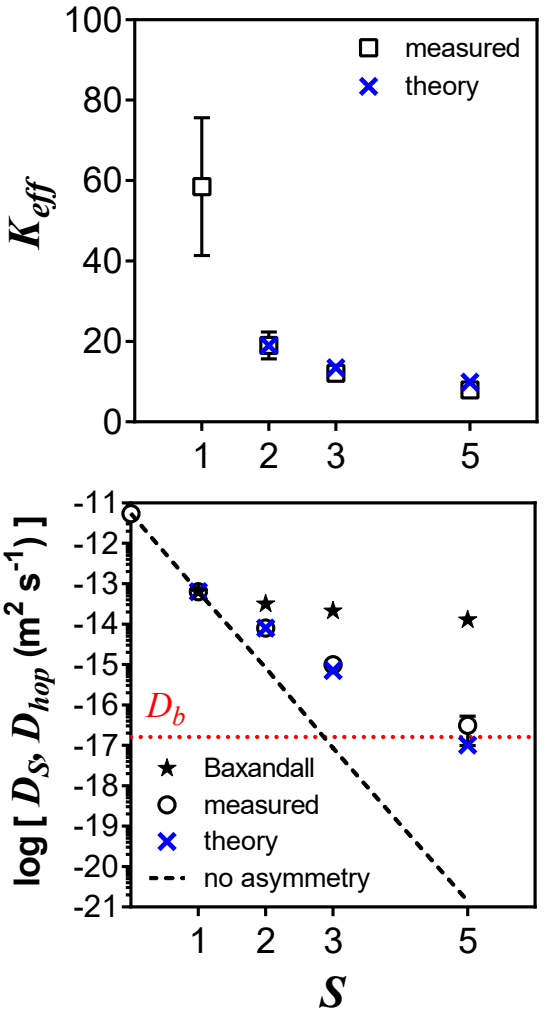

Figure 2.4. Generalized binding asymmetry for chains with multiple stickers. Measurements of K_{eff} and D_S are in good agreement with theoretical expectations of K_{eff} and $D_{hop} = p_f D_0$ from **Eq. 3** for $S = 2$, 3 and 5, generated by supplying the experimental value of $\phi_j \exp(-\beta \Delta E_B)$ measured from the single-sticker E_nP^* probe, and using $x_{min} = 0.37$ as determined for the 6-mesh concentration series. $D_b = R_{mesh}^2 / 6\tau_b = 1.61 \times 10^{-17}$ m^2 s^{-1} is the prediction for the effective mobility of network-bound chains. Results depict mean ± std. deviation from $n \geq 4$ measurements per probe.

2.7 Supporting Information

2.7.1 Materials and Methods

Plasmids construction. Cloning of all P(E_nP)$_m$ constructs was performed on a modified pQE-80L-*ΔXhoI* (≡ pX) vector (Qiagen, USA) with the native *XhoI* site upstream of the MCS inactivated by site-directed mutagenesis. Further mutagenesis was performed on pX to convert the native Asn codon immediately adjacent to the terminal stop codon (just upstream of the *HindIII* site) into a Cys codon (≡ pX*). This enabled facile generation of C-terminal cysteine versions of all proteins by shuttling them from pX to pX* with a single *BamHI* + *HindIII* double digest. The full amino acid sequences of all artificial proteins is presented in **Supplementary Table 2.2.**

Meshes and test chains of various sizes were prepared from smaller gene fragments by directed recursive ligation (**Supplementary Figure 2.2**). Genes blocks encoding proteins E_3 and P were designed and synthesized (Genscript, NJ). Each gene contained two pairs of two sequential restriction sites flanking the 5' (*BamHI-SalI*) and 3' (*XhoI-HindIII*) ends of the gene. These genes were first installed on the vector by *BamHI* + *HindIII* double digestion. Directed recursive ligation was then performed by digesting the vector (containing the gene to be extended) with *XhoI* + *HindIII*, and separately digesting the insert (extension) with *SalI* + *HindIII*. Ligation of the two digestion products between complementary *SalI-XhoI* overhangs (sites then destroyed) and *HindIII* yielded the new, chain extended gene. This cycle could be repeated as many times as desired to produce telechelic proteins of any desired size. Elastin genes were extended by iterative ligation of

the E_3 gene in the order: $E_3 > E_6 > E_{12} > E_{24} > E_{48}$. Two different sequences of the E_3 gene were used during this process to minimize the repetitiveness of the coding sequence. Each elastin gene was then capped with a P block at one end (E_nP) or both ends (PE_nP). Plasmids encoding proteins smaller than PE_6P were validated by double-stranded DNA sequencing. Plasmids encoding proteins larger than PE_6P (e.g. E_{12}^C) could not be validated this way due to the large size and highly repetitive nature of the insert. Therefore, these larger plasmids were validated by end-sequencing (partial read-through at the 5' and 3' ends to check for proper gene insertion), and the molecular weights of the gene products were then validated by ESI-MS (**Supplementary Table 2.3**).

Protein expression and purification. Plasmids coding for each proteins were transformed into BL21 chemically competent *E. coli* (NEB, Δ*fhuA2* resistant to phage T1). Overnight cultures of transformed cells were used to inoculate 1 L flasks containing Terrific Broth (TB) (inoculation ratios were typically 1:20-50) supplemented with 100 mg ml^{-1} ampicillin. Cells were grown to an OD_{600} of 0.7 – 1.0 and then induced with 1 mM isopropyl β-D-1 thiogalactopyranoside (IPTG). After 4-6 h, bacterial cultures were harvested by centrifugation for 6 min at 10,000*g*. Cells were immediately resuspended in 8 M urea, pH 8 supplemented with 100 mM phosphate, 10 mM Tris and 10 mM imidazole). Lysates were taken through two freeze-thaw cycles before being subject to high-power tip sonication (tip diameter ~ 1 cm). For sonication, 50 mL of lysate from a 1 L culture was treated at 50% maximum amplitude for 10 min in 1 sec pulse intervals (5 min total sonication time). Homogenized lysate was clarified by high-speed centrifugation (50,000*g* for 1 h) and then

subjected to standard His-tag purification over Ni-NTA agarose beads (Qiagen, USA) under denaturing conditions.

Prior to elution of the purified protein, the column was buffer-exchanged into 8 M urea supplemented with 100 mM Tris, pH 8, and eluted in this buffer with 250 mM imidazole. This allowed for removal of phosphate, and was crucial for containing soluble, well-folded batches of the smallest mesh protein (PE_3P). 50 – 100 mL of eluted protein was dialyzed against 4 L of pre-chilled distilled water at 4 °C. The water was changed repeatedly (5 – 6x) over the course of several days. For all except the largest proteins (see below), yields after lyophilization typically ranged from 80 to 200 mg/L.

The four largest proteins expressed (E_{48}^C , $E_{48}P^C$, $PE_{48}P^C$ and $P(E_6P)_4^C$) were found to be highly susceptible to proteolytic cleavage and fragmentation during the typical denaturing work-up described above. As a result, these four proteins were lysed, extracted, and purified using B-PER Complete (ThermoFisher) supplemented with "cOmplete ULTRA" protease inhibitor tablets (Roche). After extensive column washing with a native high salt buffer (100 mM Tris, 500 mM NaCl, 20 mM imidazole, pH 8), the column was exchanged into 8 M urea and washed with a step-wise pH gradient (8 > 6.3 > 5.9) before being eluted. All wash and elution fractions were analyzed, and those containing pure protein were pooled.

Fluorescent Labeling of Probes. The C-terminal cysteine of all test chains was site-specifically labeled with fluorescein-5-maleimide (Life Technologies) to permit diffusion measurements by fluorescence recovery after photobleaching (FRAP). Briefly, all probes (E_n^C, E_nP^C, PE_nP^C and multiblocks $P(E_6P)_2^C$ and $P(E_6P)_4^C$) were dissolved at 240 μM in 1

mL of 8 M urea, pH 7.5 – 8, supplemented with 100 mM NaH_2PO_4. Tris-(2-Carboxyethyl)phosphine Hydrochloride (TCEP, ThermoFisher Scientific) was added at a 20:1 ratio (TCEP:protein). After 30 min, fluorescein-5-maleimide was added at a 10:1 ratio (dye:protein), and labeling was allowed to proceed at room temperature for 2 h. Remaining thiols were then alkylated for 30 min with iodoacetamide (IAM, 20:1 ratio), and the reaction was quenched with addition of a small amount of 2-mercaptoethanol (Sigma). Tubes were gently rotated throughout the reaction. Using this procedure, the extent of polymer labeling was 0.3 moles dye per mole of protein (estimate based on comparison to dilute solutions of free dye). All fluorescently-labeled –Cys terminated proteins are denoted with a * (**Supplementary Table 2.2** and **Supplementary Figure 2.2**).

After the labeling reaction was quenched, probes were bound to a small volume of NiNTA, washed to remove unreacted dye, and then subject to a rapid on-column refolding protocol. The column was first equilibrated in a buffer containing 20 mM Tris, 100 mM NaCl, pH 7.4, and supplemented with 8 M urea, then rapidly washed in the same buffer but without urea, and eluted under native conditions (20 mM Tris, 100 mM NaCl, 500 mM imidazole). Following overnight dialysis in 100 mM phosphate buffer pH 7.4, aliquots of labeled, refolded probes were flash-frozen in liquid nitrogen and stored at -80 °C until use. Thawed probes were immediately used to prepare gels, and were photobleached within two weeks of the initial thaw.

Hydrogel Preparation. Gels were typically prepared at a concentration of 10% (*w*/*v*) (protein volume fraction $\varphi \sim 0.067$) by adding 100 mM phosphate buffer, pH 7.4, directly

to lyophilized protein. The protein was allowed to swell for several hours, and was periodically mixed and centrifuged. Fluorescent gels for FRAP experiments were prepared by swelling protein in phosphate buffer containing the desired fluorescent test chain at a concentration of ~10 μM.

Rheology. Oscillatory shear rheometry was performed on 10% (*w*/*v*) PE$_n$P meshes using an ARES-RFS strain-controlled rheometer (TA Instruments) equipped with a cone-and-plate geometry (25 mm diameter, gap width 50 μm). The outer edge of the plate was coated with mineral oil to minimize evaporation, and sample temperature was maintained at 25 °C using a circulating water batch. Strain sweeps at 10 rad s^{-1} identified a linear regime between 0.1 and 10% strain. Frequency sweeps were performed at a fixed strain amplitude of 1% between 0.01 and 100 rad s^{-1}. Large-amplitude oscillatory shear (LAOS) experiments were performed at 10 rad s^{-1} between strains of 0.1 and 1000%.

Fluorescence Recovery After Photobleaching. A small volume of fluorescent gel (5 – 10 μL) was placed between two glass coverslips separated by a 120 μm spacer (Secure-Seal Spacer, ThermoFisher). Photobleaching was performed on a Zeiss LSM 880 equipped with a 488 nm Ar-Ion laser (25 mW nominal output power) and a standard 25X/0.8NA objective. A bleach spot radius of 10 μm was defined using the Zen Black photobleaching applet, and ~1500 bleach iterations were then applied at maximum laser power and scan rate. Recovery was monitored with a wide pinhole at low laser power.

We observed variance in the effective bleach spot size and bleach depth (extent of photobleaching within a spot) among the various probes (**Supplementary Figure 2.6**).

This variance arose for several reasons: probes without stickers (e.g., the E$_n$-series) diffused very fast during the bleaching period, and had wider and shallower bleach spots as a result. Probes with one or many stickers (e.g., PE$_n$P-series) had tighter and deeper bleaches. Increasing the chain length within a given series could also change the shape of the bleach spot. Furthermore, the output power of the Ar-Ion laser steadily decreased over the experimental period by as much as 20% due to heavy use (hundreds of FRAP experiments conducted over a ~6-mo period), and decreased output power from the laser gave shallower bleaches. To control for these effects, we performed rigorous post-acquisition image analysis for each experiment:

i. The raw image stack (time series data) for each recovery was first imported into MATLAB, and the fluorescence intensity profile across the diameter of the bleach spot from the first post-bleach image was fit to a generalized Gaussian of the form:

$$g(x) \sim e^{-(|x-\mu|/\alpha)^{\beta}} \qquad \textbf{(Eq. S1)}$$

with mean μ and variance $\alpha^2\Gamma(3/\beta)/\Gamma(1/\beta)$. The variance of the bleach spot profile extracted from this fit was used as the bleach spot radius. Bleach depth (efficiency) was determined by averaging the fluorescence intensity within the area defined by this radius (**Supplementary Figure 2.6**).

ii. After measuring the bleach spot radius (variance), a spot-tracking algorithm was used to follow the center of the recovering bleach spot. The normalized

fluorescence recovery curve (range of [0,1]) was obtained by comparing the average intensity $F(t)$ in this tracked spot to the intensity in a control region of the same image $F_\infty(t)$.

$$f(t) = \frac{F(t)/F_\infty(t)}{F(t_0)/F_\infty(t_0)} \qquad \textbf{(Eq. S2)}$$

Following this normalization, the data were scaled such that $f(t_0) = 0$ using

$$\bar{f}(t) = \frac{f(t) - \min[f(t)]}{1 - \min[f(t)]} \qquad \textbf{(Eq. S3)}$$

iii. Using the MATLAB routine *nlinfit.m*, the normalized, scaled recovery traces were then fit to an effective diffusion equation derived by Soumpasis (*26, 27*):

$$\bar{f}(t) = \exp\left(\frac{-\tau_D}{2t}\right)\left[\mathrm{I}_0\left(\frac{-\tau_D}{2t}\right) + \mathrm{I}_1\left(\frac{-\tau_D}{2t}\right)\right] \qquad \textbf{(Eq. S4)}$$

where $\tau_D = a^2 / D_{eff}$. Here a is the radius of the bleach spot (the variance measured from the generalized Gaussian fit of the bleach spot profile) and $D_{eff} = D_S$ has the definition described in the main text (**Eq. 4**).

To confirm that the above procedure gave estimates for D_{eff} that were not affected by the output laser power, or intrinsically biased by the fast or slow recovery rate of the probe (which could change the bleach efficiency and the shape of the bleach spot), we acquired 173 control FRAP traces across the four different meshes (3-, 6-, 12-, and 24-mesh), using matched (N = M) E$_n$-series probes at two labeling concentrations (ca. 1 and 10 μM)

(**Supplementary Figure 2.7**). The bleach efficiency and effective bleach spot size were systematically varied by increasing the duration of the bleach period (# of bleach iterations). The effective mobilities $D_{eff} = D_S$ obtained from this dataset using the analysis described above were independent of the bleach efficiency, bleach spot size, and probe concentration (**Supplementary Figure 2.7**). Specifically, the standard deviation of D_{eff} across the different bleach efficiencies did not exceed 25% of the mean D_{eff} for any of the probe concentrations and mesh sizes examined ($0.14 < \mu / \sigma < 0.25$).

2.7.2 Supplementary Equations and Derivations

Estimation of key *n*-mesh parameters. The characteristic dimensions of differently sized meshes were estimated from protein concentration, simple geometric arguments, and molecular weight data. First, the number density of junctions n_j (crosslinking sites) was calculated as

$$n_j = \frac{2}{5}\left(\frac{\rho}{M}\right)N_A \qquad \textbf{(Eq. S5)}$$

where ρ is the protein mass concentration in g/L, M is the molecular weight of the mesh, and N_A is Avogadro's number. From **Eq. S5**, the characteristic mesh size R_{mesh} was estimated by approximating the average distance between junctions as two times the radius of a sphere with the volume equal to the mean volume per junction.

$$R_{mesh} = 2 \times \left(\frac{3}{4\pi n_j}\right)^{1/3} \qquad \textbf{(Eq. S6)}$$

Values of R_{mesh} obtained from **Eq. S6** are reported in **Supplementary Table 2.4**. To estimate ϕ_j, the fractional volume accessible to dangling chains, we use

$$\phi_j = \frac{\bar{\upsilon}_p}{\frac{1000}{\rho_j} + \bar{\upsilon}_p} \approx \bar{\upsilon}_p \left(\frac{\rho_j}{1000} \right) \qquad \textbf{(Eq. S7)}$$

where $\bar{\upsilon}_p = 0.7230$ mL/g is the partial specific volume of the protein estimated from elastin sequence data and the mean volume of each amino acid residue (*34*). Here ρ_j is the junction mass concentration, which is related to the total protein concentration by M_P / M_{PEP}, the molecular weight ratio of the P domain to the whole protein.

$$\rho_j = \rho \left(\frac{2M_P}{M_{PEP}} \right) \qquad \textbf{(Eq. S8)}$$

Since $\phi_j = n_j \upsilon_j$ and $\upsilon_j = 4\pi c^3 / 3$, **Eq. S5** and **S7** provide an estimate for $c = 1.89$ nm, the average dimension of a cluster. This is in good agreement with structural data on the P domain, since $c = 2.31$ nm is provided by the X-ray crystal structure of the pentameric assembly (*35*). In order to make quantitative comparisons of experimental data to predictions from **Eq. 1** and **Eq. 2**, we numerically specified $\phi_j = n_j \upsilon_j$ in terms of c and the mesh size R_{mesh}:

$$\phi_j = \left(\frac{2c}{R_{mesh}} \right)^3 \qquad \textbf{(Eq. S9)}$$

Generalized binding asymmetry for multisticker probes. Consider the case of a chain with S = 3 evenly spaced stickers along its backbone, with $j = 2$ blocks of molecular weight N and Kuhn length b (**Supplementary Figure 2.1**). For $i = 0$, there is only $N_b = 1$ state (the free state with all stickers unbound), and $Z_0 = Q_0 = G_f{}^2$, where G_f takes the same form as for telechelics. For $i = 1$ there are $N_b = 3$ possible bound states, and binding restricts the chain to a fraction of the total system volume ϕ_j. Assuming no loss of conformational entropy during this single sticking event provides $\sum_{k=1}^{3} Q_k = \sum_{k=1}^{3} \phi_j G_{k,1} G_{k,2} = 3\phi_j G_f{}^2$. Thus from **Eq. 3**, $K_1 = 3\phi_j \exp(-\beta \Delta E_B)$ for a 3-sticker chain. Note that this is $3/2$ the value of a 2-sticker (telechelic) chain, which arises as a direct consequence of the extra sticker.

Similar to telechelics, states with $i = 2$ bound blocks must pay the entropic cost associated with simultaneously locating two well-spaced junctions, or else form loops. The entropy for a chain with two adjacent bound stickers and one dangling end (see k = 2,3 in **Supplementary Figure 2.1**) is $Q_2 = Q_3 = \phi_j{}^2 G_f G_b$, where again $\phi_j G_b = \phi_j G_B + G_L$ as for telechelics. For the state with one unbound sticker in the middle (k = 1), the conformations of each block are coupled. We use the self-similarity property of Gaussian chains to write $Q_1 = \phi_j{}^2 G_b(\mathbf{R}; 2N, b) = \phi_j{}^2 G_b(2N)$, i.e., the chain is effectively telechelic with a block length of 2N. Summing over all k we obtain $Z_2 = \phi_j{}^2 (2Q_{2,3} + Q_1)$, and together with Z_1, that $K_2 = \dfrac{2G_f G_b + G_b(2N)}{3G_f{}^2} \phi_j \exp(-\beta \Delta E_B)$. When all three stickers are bound (i = 3), there is again only one possible state. In this case $Z_3 = \phi_j{}^3 G_b{}^2$, and the equilibrium constant is

$K_3 = \frac{{G_b}^2}{2G_f G_b + G_b(2N)} \phi_j \exp(-\beta \Delta E_B)$. Analogous combinatorial considerations provide each K_i for chains with even more stickers. The results for the case of $S = 5$ are presented in **Supplementary Table 2.1**.

Evaluation of configurational integrals. Eq. 1 and **Eq. 2** in the main text specify K_1 / K_2 in terms of the following configurational integrals:

$$G_f = \int_0^\infty p(\mathbf{R}) d\mathbf{R} = 4\pi \int_0^\infty p(R) R^2 dR = 1 \qquad \textbf{(Eq. S10)}$$

$$G_L = \int_0^l p(\mathbf{R}) d\mathbf{R} = 4\pi \int_0^l p(R) R^2 dR \qquad \textbf{(Eq. S11)}$$

$$G_B = \int_0^\infty p(\mathbf{R}) g(\mathbf{R}) d\mathbf{R} = 4\pi \int_0^\infty p(R) g(R) R^2 dR \qquad \textbf{(Eq. S12)}$$

where $l \sim O(b)$ represents the end-to-end distance of a looped chain, and we approximate $g(R)$ as a Heaviside step function activated at $R = R_{mesh}$. Since $R_{mesh} \sim \phi_j^{-1/3}$, $g(R; R_{mesh})$ has an implicit dependence on ϕ_j. Evaluation of the above integrals requires a choice of $p(R)$, which we choose to be the Gaussian chain integral:

$$p(R) = (3 / 2\pi N b^2)^{3/2} \exp(-3R^2 / 2Nb^2) \qquad \textbf{(Eq. S13)}$$

Selection of limits on the looping integral. Because **Eq. 1** in our theory predicts the fraction of bridged and looped chains [B] and [L], it is possible to compare the theoretical fraction of bridged chains to the fraction of elastically effective chains $G'_\infty / G_{phantom}$ estimated from rheology and phantom network theory (**Supplementary Figure 2.11**). For

a given cluster dimension *c*, this constraint fixes the limits of the looping integral *l*. Recall the definitions of each equilibrium constant, and the assumption that $G_d \approx 2G_f$:

$$K_1 = \frac{[d]}{[f]} = \frac{\phi_j G_d}{G_f} \exp(-\beta \Delta E_B) = 2\phi_j \exp(-\beta \Delta E_B)$$

$$K_L = \frac{[L]}{[d]} = \frac{G_L}{2G_d} \exp(-\beta \Delta E_B) = K_1 G_L / 4\phi_j$$

$$K_B = \frac{[B]}{[d]} = \frac{\phi_j G_B}{2G_d} \exp(-\beta \Delta E_B) = K_1 G_B / 4$$

If we require the normalization $[f]+[d]+[B]+[L]=1$, then $[B] = G'_\infty / G_{phantom}$ is exact and we need only solve for $[B]$ in terms of known equilibrium constants.

$$\frac{[d]}{K_1} + [d] + K_L[d] + [B] = 1$$

$$\left(\frac{1}{K_1} + 1 + K_L\right)[d] + [B] = 1$$

$$\left(\frac{1}{K_1} + 1 + K_L\right)\frac{[B]}{K_B} + [B] = 1$$

$$[B] = \left[1 + \frac{1}{K_B}\left(K_L + 1 + \frac{1}{K_1}\right)\right]^{-1}$$

$$[B] = \left[1 + \frac{1}{G_B}\left(G_L(l)/\phi_j + \frac{4}{K_1} + \frac{4}{K_1{}^2}\right)\right]^{-1} \qquad \textbf{(Eq. S14)}$$

Assuming $K_1 \gg 1$, the above expression simplifies to:

$$[B] = \left[1 + \frac{G_L(l)}{\phi_j G_B}\right]^{-1} = f(l; R_{mesh}, N, b, c) = G'_\infty / G_{phantom} \qquad \textbf{(Eq. S15)}$$

Eq. S14 or **Eq. S15** may be used to fix $l = l_{calc}$ provided that reasonable estimates of the mesh parameters (R_{mesh}, c) are known and the polymer is properly coarse-grained as an equivalent, freely-jointed chain (N, b). Representative plots of $G'_\infty / G_{phantom}$ versus l are shown in **Supplementary Figure 2.11**, and the $x_{calc} = l_{calc} / c$ values obtained using this scheme are presented in **Supplementary Table 2.4**.

An inverse use of this framework is the calculation of the fraction of loops from a measurement of $G'_\infty / G_{phantom} = [B]$. It is easy to show that this provides $[L]$ in a straightforward manner, provided K_1 and l are known in advance:

$$[L]\left(\frac{1}{K_L K_1} + \frac{1}{K_L} + 1\right) = 1 - G' / G_{phantom}$$

$$[L] = \frac{1 - G' / G_{phantom}}{\frac{4\phi_j}{K_1^2 G_L(l)} + \frac{4\phi_j}{K_1 G_L(l)} + 1} \qquad \textbf{(Eq. S16)}$$

We obtain K_1 from FRAP measurements, and $l = l_{min}$ from minimizing residuals (**Supplementary Figure 2.11**), although in the absence of such information it is also possible to simply take $l \approx b$. Values of $[L]$ in each n-mesh obtained using K_1 and l_{min} are

also presented in **Supplementary Table 2.11**. Note that **Eq. S15** collapses to the well-known equation $[L] \approx 1 - G'/G_{phantom}$ for very large K_1.

2.7.3 Supplementary Tables

Supplementary Table 2.1. Exact equilibrium constants for a multisticker probe with S = 5 stickers. Each K_i is normalized by the factor $\phi_j \exp(-\beta\Delta E_B)$, and the numerical data for each K_i / K_{i-1} were calculated using coarse-grained data on the 6-mesh network, i.e. b = 0.95 nm and N = 72, but with R_{mesh} adjusted to be 14.06 nm such that K_1 / K_2 = 55.6 for telechelics is predicted exactly (x = 0.37 was used for the looping integral based on minimization of the residuals in the 6-mesh concentration series). G_b and G_f take the same form as for telechelics, and unless otherwise noted, $G_b = G_b(N)$ where N is the length of an equivalent freely joined chain between each sticker.

	$K_i / \phi_j \exp(-\beta\Delta E_B)$	K_i / K_{i-1}
$i = 1$	5	-
$i = 2$	$\frac{G_b(4N) + 2G_b(3N)G_f + 3G_b(2N)G_f^2 + 4G_bG_f^3}{5G_f^4}$	0.091
$i = 3$	$\frac{3G_b^2G_f^2 + 4G_b(2N)G_bG_f + 2G_b(3N)G_b + G_b(2N)^2}{G_b(4N) + 2G_b(3N)G_f + 3G_b(2N)G_f^2 + 4G_bG_f^3}$	0.181
$i = 4$	$\frac{2G_b^3G_f + 3G_b(2N)G_b^2}{3G_b^2G_f^2 + 4G_b(2N)G_bG_f + 2G_b(3N)G_b + G_b(2N)^2}$	0.276
$i = 5$	$\frac{G_b^5}{2G_b^3G_f + 3G_b(2N)G_b^2}$	0.020

Supplementary Table 2.2. Sequences of all probe and mesh proteins prepared by directed recursive ligation. All mesh proteins were encoded on a pQE-80L-*ΔXhoI* (≡ pX) plasmid backbone, and all –Cys terminated proteins (used to prepare the * fluorescent probes) were encoded on a pQE-80L-*ΔXhoI*-Cys vector (≡ pX^*).

Protein	MW (Da)	Sequence
P		APQMLRE LQETNAA LQDVREL LRQQVKE ITFLKNT VMESDAS
E_n		$[(VPGAG)_2VPGEG(VPGAG)_2]_n$
E_n* series		MRGSH$_6$GSVD-{**insert**}-LEH$_6$KLC
E_3^C	8,936	**E_3**
E_6^C	15,060	**E_3**-LD-**E_3**
E_{12}^C	27,308	[**E_3**-LD]$_3$-**E_3**
E_{24}^C	51,805	[**E_3**-LD]$_7$-**E_3**
E_{48}^C	100,798	[**E_3**-LD]$_{15}$-**E_3**
E_nP* series		MRGSH$_6$GSVD-{**insert**}-(GS)$_6$G-**P**-(GS)$_6$-LEH6KLC
E_3P^C	15,779	**E_3**-LD
E_6P^C	21,903	[**E_3**-LD]$_2$
$E_{12}P^C$	34,151	[**E_3**-LD]$_4$
$E_{24}P^C$	58,647	[**E_3**-LD]$_8$
$E_{48}P^C$	107,640	[**E_3**-LD]$_{16}$
PE_nP* series		MRGSH$_6$GSVD(GS)$_6$G-**P**-(GS)$_6$LD-{**insert**}-(GS)$_6$G-**P**-(GS)$_6$-LEH6KLC
PE_3P^C	22,621	**E_3**-LD
PE_6P^C	28,745	[**E_3**-LD]$_2$
$PE_{12}P^C$	40,994	[**E_3**-LD]$_4$
$PE_{24}P^C$	65,490	[**E_3**-LD]$_8$
$PE_{48}P^C$	114,483	[**E_3**-LD]$_{16}$
mesh series		MRGSH$_6$GSVD(GS)$_6$G-**P**-(GS)$_6$LD-{**insert**}-(GS)$_6$G-**P**-(GS)$_6$-LEH$_6$KLN
PE_3P "3-mesh"	22,632	**E_3**-LD
PE_6P "6-mesh"	28,756	[**E_3**-LD]$_2$
$PE_{12}P$ "12-mesh"	41,004	[**E_3**-LD]$_4$
$PE_{24}P$ "24-mesh"	65,501	[**E_3**-LD]$_8$
$P(E_nP)_m$* series (multistickers)		
E_6^C	15,060	MRGSH$_6$GSVD-**E_3**-LD-**E_3**-LEH$_6$KLC
E_6P^C	21,903	MRGSH$_6$GSVD-[**E_3**-LD]$_2$-(GS)$_6$G-**P**-(GS)$_6$-LEH$_6$KLC
PE_6P^C	28,745	MRGSH$_6$GSVD(GS)$_6$G-**P**-(GS)$_6$LD-[**E_3**-LD]$_2$-(GS)$_6$G-**P**-(GS)$_6$-LEH$_6$KLC
$P(E_6P)_2^C$	47,836	MRGSH$_6$GSVD(GS)$_6$G-**P**-(GS)$_6$-{LD-[**E_3**-LD]$_2$-(GS)$_6$G-**P**-(GS)$_6$}$_2$-LEH$_6$KLC
$P(E_6P)_4^C$	86,018	MRGSH$_6$GSVD(GS)$_6$G-**P**-(GS)$_6$-{LD-[**E_3**-LD]$_2$-(GS)$_6$G-**P**-(GS)$_6$}$_4$-LEH$_6$KLC

Supplementary Table 2.3. ESI-MS data for large *n*-probes. The remaining proteins (PE_6P and smaller) were validated by double-stranded DNA sequencing of the corresponding plasmid. All –Cys terminated proteins were blocked with iodoacetamide (+IAM, Δ = +57 Da) prior to analysis.

Protein	Predicted (Da)	+IAM (Da)	Observed (Da)	% error
E_{12}^C*	27,308	27,365	27,319	0.167%
$E_{12}P^C$	34,151	34,208	34,211	0.009%
$PE_{12}P^C$	40,994	41,051	41,043	0.019%
$PE_{12}P$	41,004	-	41,021	0.042%
E_{24}^C	51,805	51,862	51,867	0.010%
$E_{24}P^C$	58,647	58,704	58,710	0.010%
$PE_{24}P^C$	65,490	65,547	65,552	0.008%
$PE_{24}P$	65,501	-	65,506	0.007%
E_{48}^C	100,798	100,855	100,862	0.007%
$E_{48}P^C$	107,640	107,697	107,702	0.005%
$PE_{48}P^C$	114,483	114,540	114,573	0.029%
$P(E_6P)_2^C$	47,847	47,904	47,906	0.004%
$P(E_6P)_4^C$	86,018	86,075	86,080	0.006%

**observed by MALDI*

Supplementary Table 2.4. Experimental parameters and exponent data for *n*-mesh. *M* represents the true molecular weight of each *n*-mesh (including P domains). The mesh size was calculated as $R_{mesh} = 2\left(3/4\pi n_j\right)^{1/3}$, i.e. two times the radius of a sphere with a volume equal to the mean volume per site. A cluster dimension of c = 1.89 nm was taken for calculating l, the bounds of the looping integral G_L. The fraction of elastically effective chains, $G'_\infty / G_{phantom}$, is the average value measured from rheology ($n \geq 2$ independent measurements) with $G_{phantom} = \rho RT(1-2/f)/M$, where f = 5 for a pentameric network junction. Each a_s and β_i represent the molecular weight exponents calculated from power-law fits to the diffusivity data in **Supplementary Figure 2.9**. $x_{calc} = l_{calc}/c$ was determined from **Eq. S15** using the experimental $G'/G_{phantom}$ and the coarse-grained values of N and b for each mesh (**Supplementary Table 2.5**). Each $x_{min} = l_{min}/c$ was used to generate the master plot in **Figure 2.2D**, and was determined from minimizing the residuals between K_1/K_2 and **Eq. 1** in each mesh (**Supplementary Figures 2.11** and **2.12**). $[B]$ and $[L]$ were determined from **Eq. S14** and **S16** respectively using x_{min}.

	3-mesh	6-mesh	12-mesh	24-mesh
M (Da)	22,632	28,756	41,004	65,501
R_{mesh} (nm)	12.2	13.2	14.8	17.3
$G'_\infty/G_{phantom}$	0.59	0.74	0.82	0.67
x_{calc} (nm)	0.15	0.28	0.42	0.80
x_{min} (nm)	0.24	0.26	0.43	0.35
$[B]$	0.11	0.49	0.66	0.79
$[L]$	0.13	0.07	0.08	0.05
	$D_S \sim N^{\alpha}$, $K_i \sim N^{\beta}$			
α_0	-1.4 ± 0.1	-1.5 ± 0.0	-1.4 ± 0.1	-1.3 ± 0.1
α_1	-1.0 ± 0.1	-0.9 ± 0.1	-1.0 ± 0.1	-1.0 ± 0.1
α_2	-1.6 ± 0.1	-1.5 ± 0.1	-1.3 ± 0.2	-1.4 ± 0.1
$\beta_1 = \alpha_0 - \alpha_1$	-0.4 ± 0.1	-0.6 ± 0.1	-0.4 ± 0.1	-0.3 ± 0.1
$\beta_2 = \alpha_1 - \alpha_2$	0.6 ± 0.2	0.6 ± 0.1	0.3 ± 0.2	0.4 ± 0.1
$\beta_1 - \beta_2$	-1.0 ± 0.2	-1.2 ± 0.1	-0.7 ± 0.2	-0.7 ± 0.2

Supplementary Table 2.5. Coarse graining of probe size based on the Flory characteristic ratio C_∞ = 2.51 (*28*). The value n_p reflects the number of peptide bonds between each P domain on PE$_n$P-type probes. The molecular weight of this inter-sticker region ("MW$_{eff}$") is also shown. $R_{probe} = (C_\infty n_p l_p)^{1/2} = bN^{0.5}$ and $R_{max} = n_p l_p$ were calculated taking l_p = 0.380 nm as the "virtual" length of each peptide bond (linear C_α–C_α distance). The length of a Kuhn monomer is $b = C_\infty n_p l_p^2 / R_{max}$, and the equivalent freely jointed chain is composed of $N = R_{max}^2 / C_\infty n_p l_p^2$ such monomers, each with an effective molar mass of M_0 (*25*). The parameters calculated below were also used to estimate various mesh parameters in **Supplementary Table 2.4**, assuming "size-matched" networks ($N = M$).

	MW_{eff} (Da)	n_p	R_{probe} (nm)	R_{max} (nm)	b (nm)	N	M_0 (Da)
3-probe	8,121	104	6.1	39.5	0.95	41	196
6-probe	14,245	181	8.1	68.8	0.95	72	198
12-probe	26,493	335	11.0	127.3	0.95	133	199
24-probe	50,990	643	15.3	244.3	0.95	256	199
48-probe	99,982	1259	21.4	478.4	0.95	502	199

2.7.4 Supplementary Figures

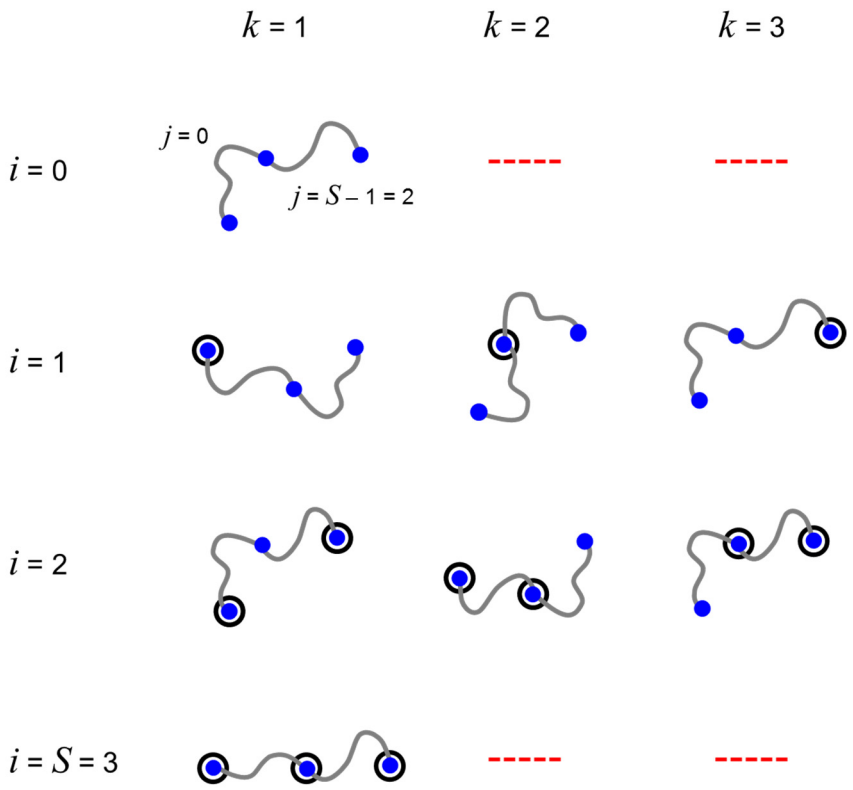

Supplementary Figure 2.1. Schematic of all possible binding configurations of a chain with *S* = 3 stickers. The chain has $k \leq C(S,i)$ possible bound states for each $i \leq S$ number of bound stickers, where $C(S,i)$ is the binomial coefficient. The sum $j = S-1$ runs over the total number of independent blocks.

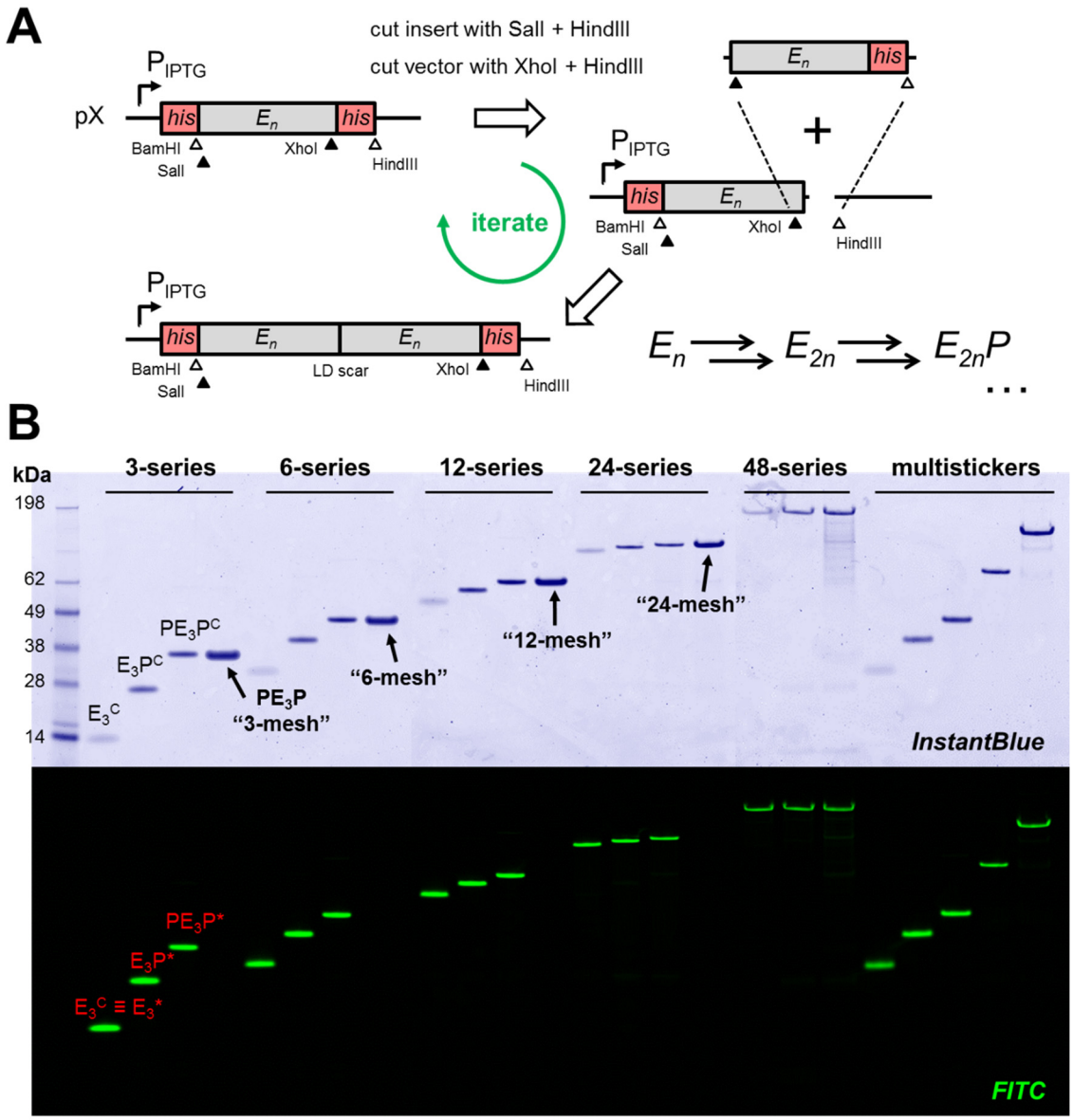

Supplementary Figure 2.2. Outline of cloning scheme (recursive directed ligation). (**A**) To perform chain extension, a "pX ≡ pQE-80L-*ΔXhoI*" is cut with *Sal*I and *Hind*III, and an insert is cut with *Xho*I and *Hind*III. Ligation of the insert and vector produces the chain extended product with the same four sites on the new vector. The internal *Sal*I-*Xho*I site is destroyed during the ligation, generating an "LD" scar. (**B**) SDS-PAGE gels of the 21 unique artificial proteins prepared by this method (full sequences are presented in **Supplementary Table 2.2**). All FRAP probes were site-specifically labeled at their C-terminal Cys residue with fluorescein-5-maleimide (the labeled -Cys terminated proteins are denoted with *).

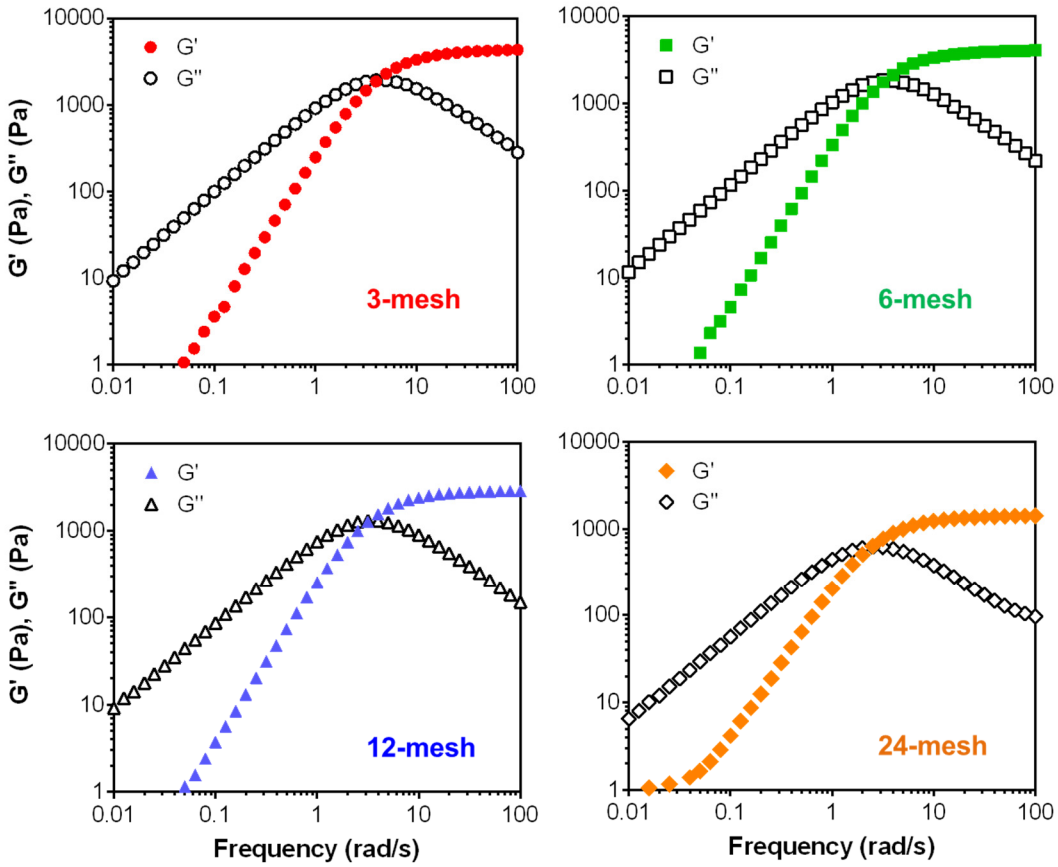

Supplementary Figure 2.3. Linear oscillatory shear rheology of hydrogels with varying mesh sizes. Hydrogels were prepared by swelling lyophilized mesh proteins in 100 mM phosphate buffer, pH 7.4, at a concentration of 10% (*w*/*v*). Frequency sweeps were performed at a fixed strain amplitude of 1% between 0.01 and 100 rad s^{-1}.

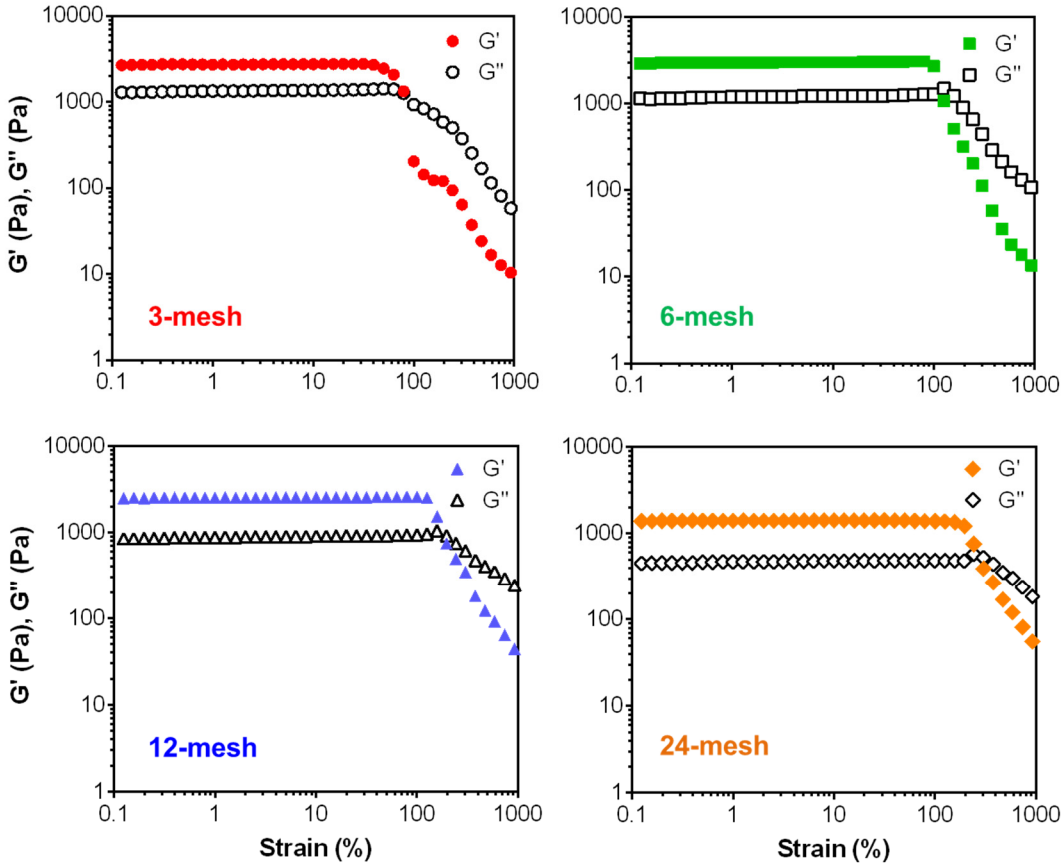

Supplementary Figure 2.4. Non-linear rheology of hydrogels (LAOS) with varying mesh sizes. Large-amplitude oscillatory shear was performed on 10% hydrogels at 10 rad s^{-1} between 0.1 and 1000% strain. At a fixed protein concentration, larger meshes have an increased critical strain (yield strain), as well as a decreased yield stress (**Supplementary Figure 2.5**).

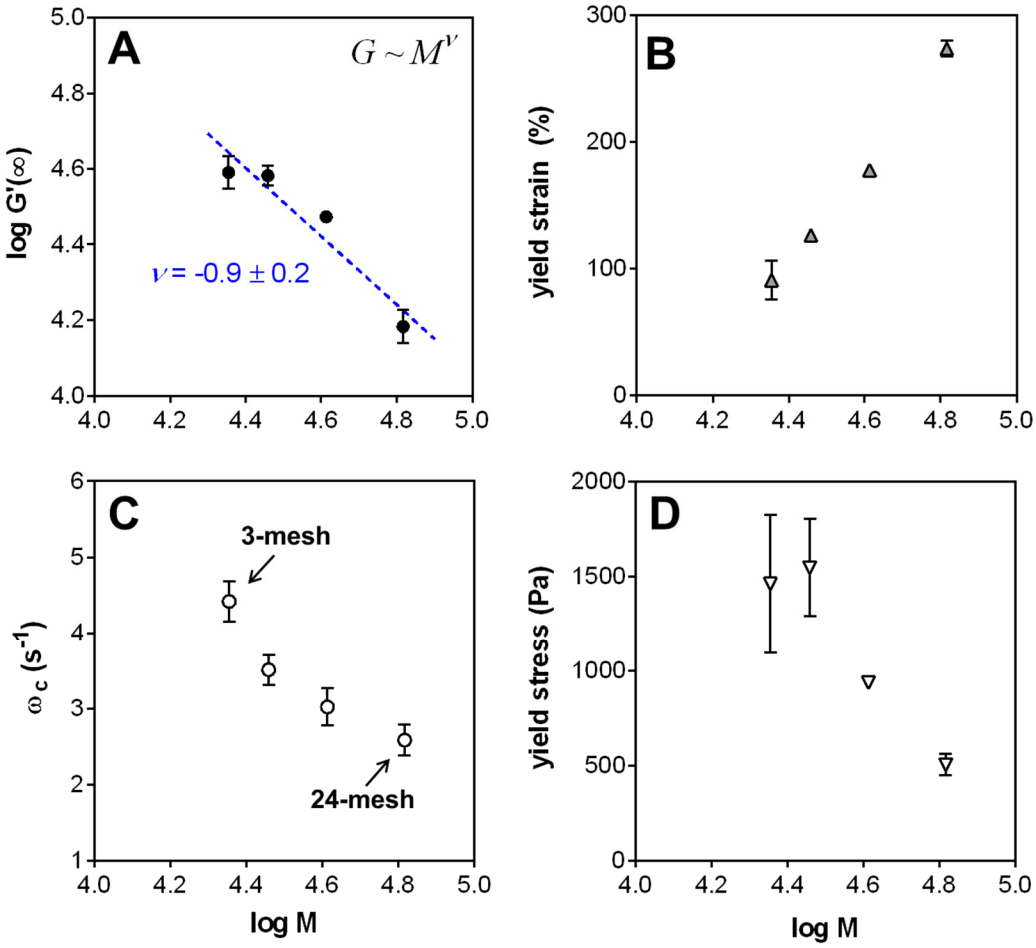

Supplementary Figure 2.5. Summary of rheological properties of hydrogels with varying mesh sizes. Networks were prepared at a fixed protein concentration of 10% (*w*/*v*) in 100 mM phosphate buffer, pH 7.4 (points in each graph represent μ ± σ for 2 – 3 independent gel preparations). (**A**) The terminal storage modulus $G'(\infty)$ (taken as $G'(100)$ from **Supplementary Figure 2.3**) follows the molecular weight dependence expected from rubber elasticity theory $(G' = \rho RT / M)$. (**B**) Gels with larger meshes have a greater terminal strain. Terminal strain is taken as the point at which $G' = G''$ in the LAOS curve (**Supplementary Figure 2.4**). (**C**) The network relaxation rate (crossover frequency, ω_c) shows a weak dependence on mesh size. The crossover frequency is taken as the point at which $G' = G''$ in the frequency sweep (**Supplementary Figure 2.3**). (**D**) Larger meshes have an apparently lower yield stress.

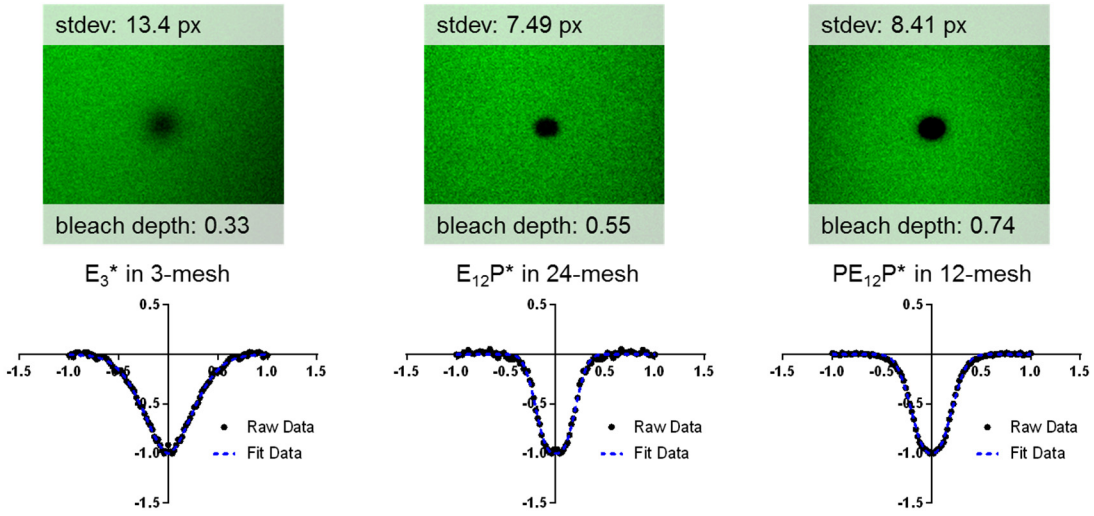

Supplementary Figure 2.6. Variable bleach spot profiles for different probes. (*Top*) Shown are representative post-bleach images for several probes in several different meshes. (*Bottom*) To control for this variance, the fluorescence intensity profile across the bleach spot was fit to a generalized Gaussian, and the spot size information was supplied to a tracking algorithm that extracted the normalized fluorescence recovery curves. The spot size information from the fit was also supplied during the estimation of $D_{eff} = D_S$.

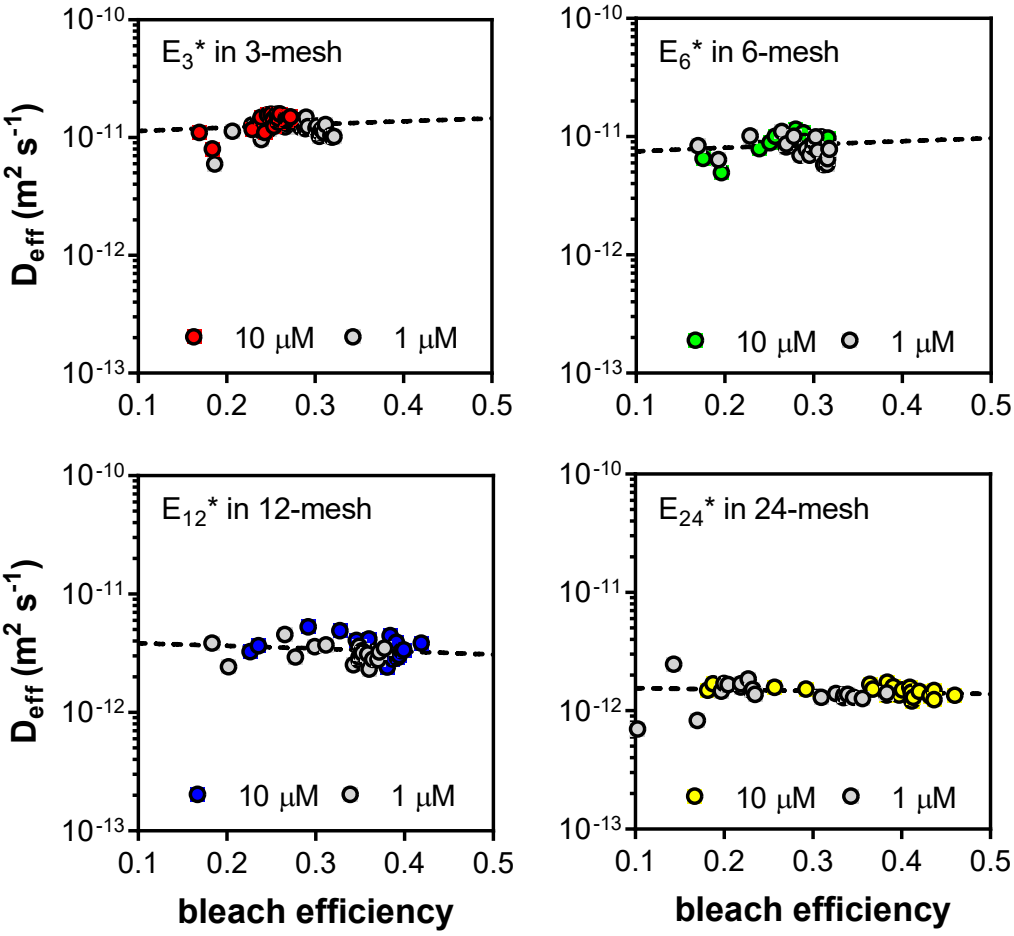

Supplementary Figure 2.7. Validation of the FRAP analysis procedure in different meshes. 173 control FRAP traces were acquired for four test chains in size-matched ($N = M$) meshes at varying bleach efficiencies and two different probe concentrations. The effective mobilities $D_{eff} = D_S$ obtained from this dataset are independent of the bleach efficiency, bleach spot size, and probe concentration. Dashed lines show linear regressions to D_{eff} versus bleach efficiency for both probe concentrations within each mesh. No regression line has a slope significantly different from zero ($P > 0.33$). Moreover, for a given probe concentration within each mesh, the standard deviation of D_{eff} across the different bleach efficiencies does not exceed 25% of the mean D_{eff} (i.e., $0.14 < \mu / \sigma < 0.25$).

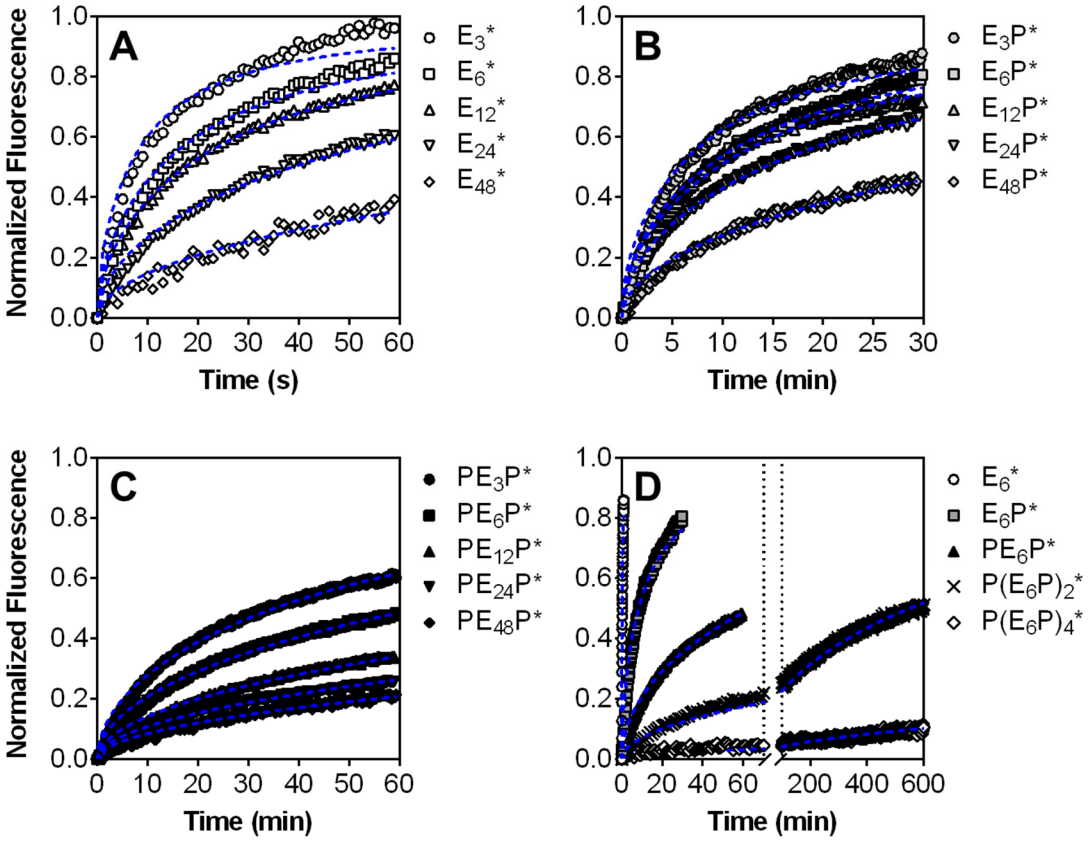

Supplementary Figure 2.8. Representative FRAP recovery curves in "6-mesh" networks. Fluorescent probes of various sizes, and with different numbers of associative domains ("stickers") were used to label 10% PE_6P hydrogels (probe concentration ~ 10 μM), then photobleached. Fluorescence recovery was monitored for varying lengths of time, typically until at least ~50% of the original intensity was restored (within 1 – 2 h for most probes). Shown are recovery traces for (**A**) E_n* probes, (**B**) E_nP* probes, (**C**) PE_nP* probes, and (**D**) $P(E_nP)_m$* multisticker probes. Each recovery trace was fit to **Eq. S4**, which allowed the effective diffusivity $D_{eff} = D_S$ to be determined using **Eq. 4**.

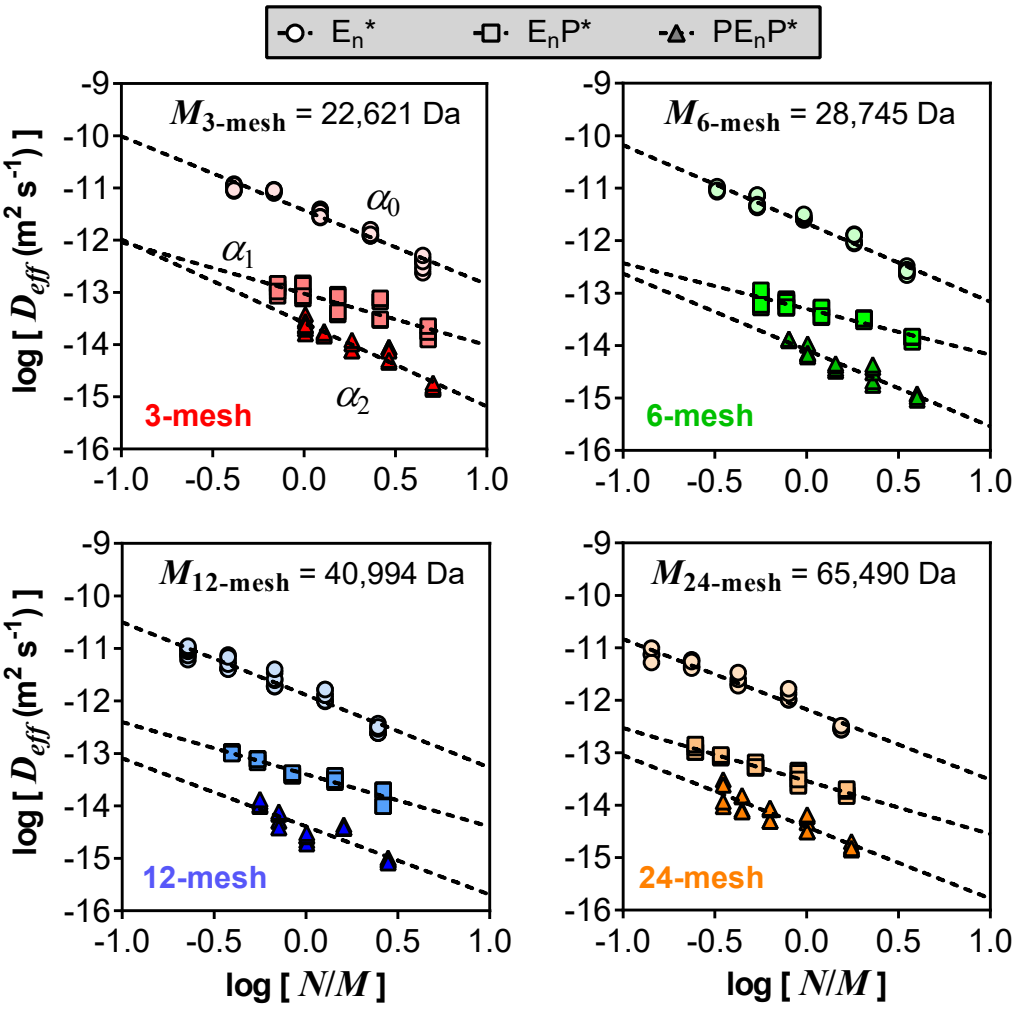

Supplementary Figure 2.9. Molecular weight dependence of D_S for probes in different meshes Shown are 298 effective diffusivities for each probe, determined from fits to FRAP traces (**Supplementary Figure 2.8**, $n \geq 4$ measurements per probe, per mesh). Power-law fits were used to determined molecular weight scaling of each probe series, and the exponents for these fits are presented in **Supplementary Table 2.4**. As described in the main text, each probe series determines a different D_S: D_0 (E_n*), D_1 (E_nP*), and D_2 (PE_nP*).

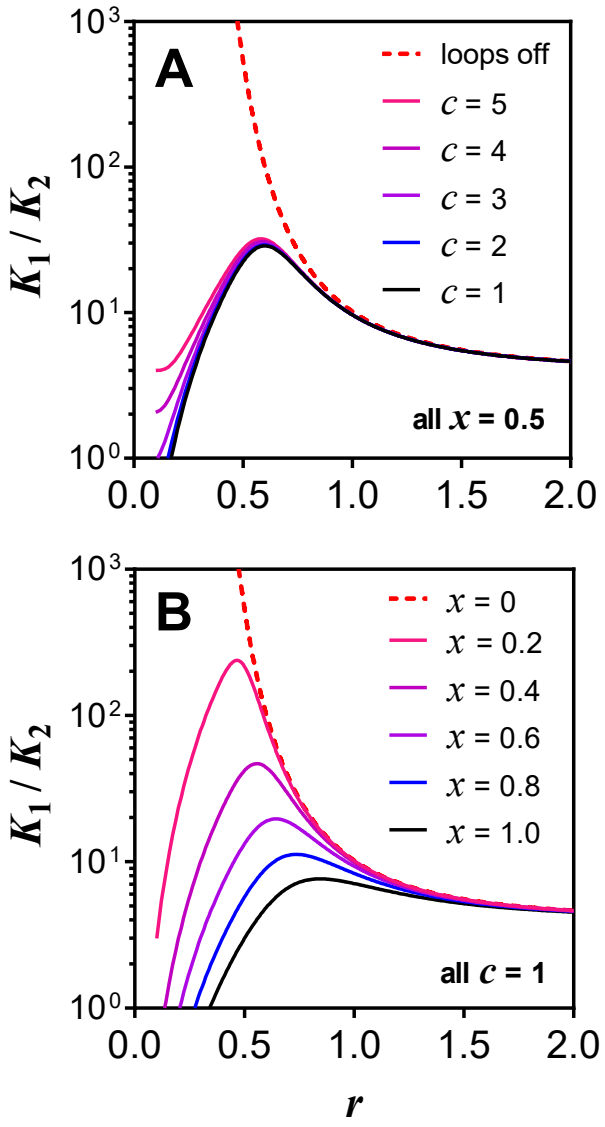

Supplementary Figure 2.10. Independence of Eq. 1 on *c* for fixed *x* = *l* / *c*. (**A**) The cluster dimension was taken to be $c = 1 – 5$, $R_{mesh} = 10$, $b = 1$, and x was fixed at 0.5. Shown are predictions for K_1 / K_2 for each of these five cases from **Eq. 1**, along with **Eq. 2** for the "loops off" case. The behavior of **Eq. 1** is insensitive to the choice of c for $c < R_{mesh}$. (**B**) For a fixed cluster size of $c = 1$, the limits of the looping integral (specified by $x = l / c$) determine the behavior of **Eq. 1**.

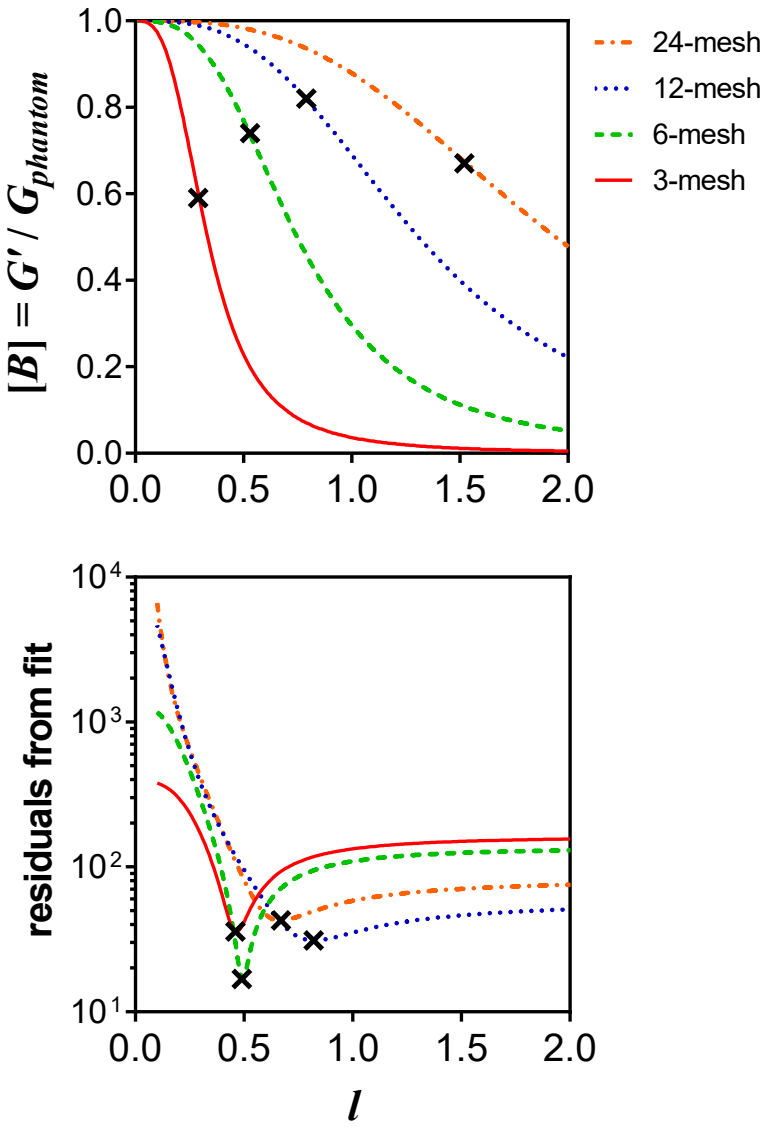

Supplementary Figure 2.11. Selection criteria for the limits of the looping integral. We expect $l \sim O(b)$ such that $x = l/c \approx 0.5$ from c = 1.89 nm where b = 0.95 nm. (*Top*) Matching the experimental fraction of elastically effective chains to predictions from **Eq. S15** fixes this limit precisely, providing x_{calc} for each mesh. (*Bottom*) Alternatively, minimizing the K_1 / K_2 residuals from **Eq. 1** in each mesh (**Supplementary Figure 2.12**) provides x_{min}. The calculated and residuals-minimized x values are all ≈ 0.5 as expected.

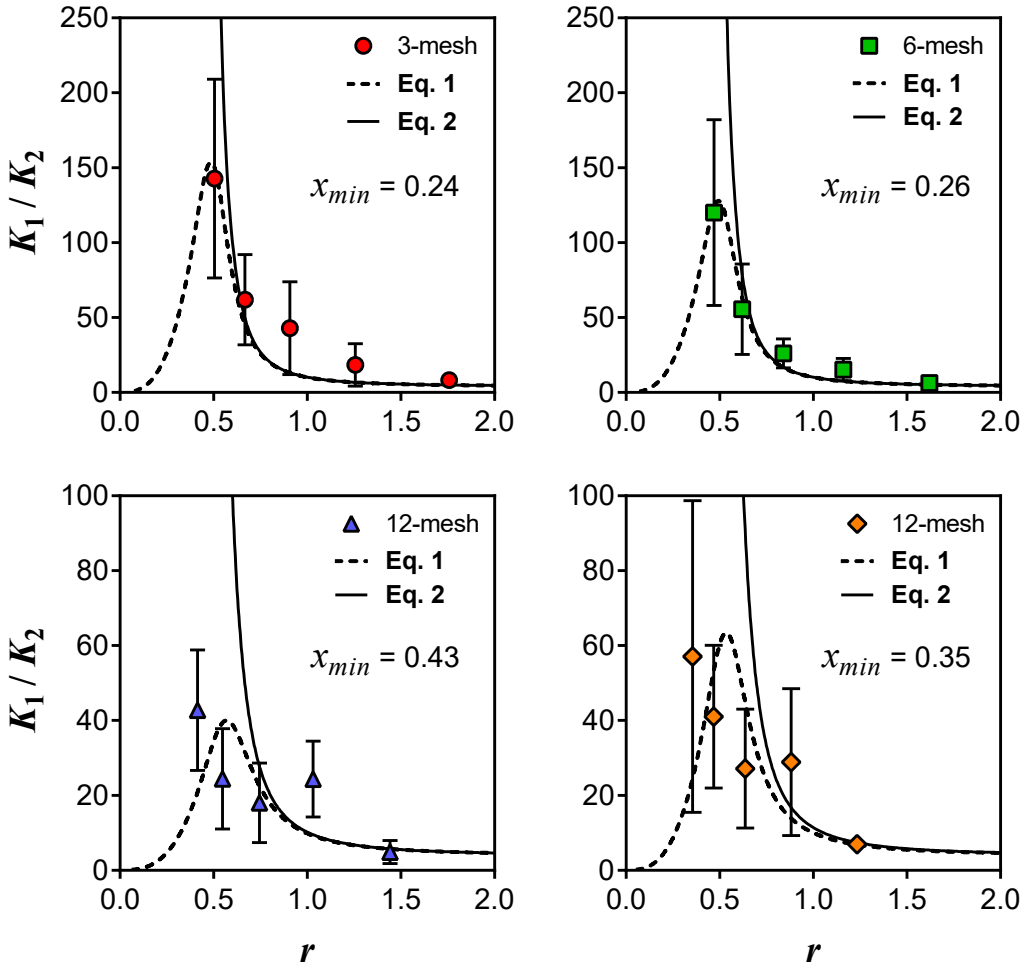

Supplementary Figure 2.12. Minimized K_1 / K_2 residuals in each mesh, analogous to Figure 2.3D. The values of $x_{min} = l_{min} / c$ determined in **Supplementary Figure 2.11** were used to plot **Eq. 1**, along with the coarse-grained data (b, N, R_{mesh}) on each mesh shown in **Supplementary Tables 2.4** and **2.5**.

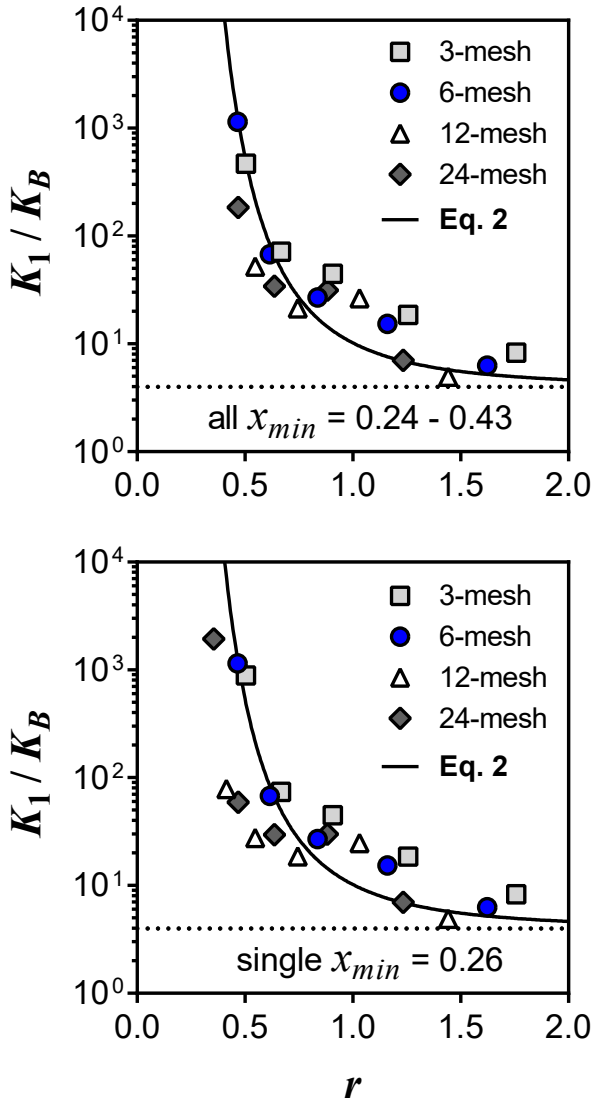

Supplementary Figure 2.13. A single choice of x_{min} = 0.26 is sufficient to collapse the binding data in each mesh onto Eq. 2 (*Bottom*), although the fit is slightly improved by selecting x_{min} differently in each mesh (*Top*, same as **Figure 2.3D**). The top plot summarizes 271 measurements (out of 298 total, loops are overestimated at 2 of 20 probe-mesh ratios), whereas the bottom curve contains all 298 measurements, but underestimates looping contributions in the 12- and 24-mesh.

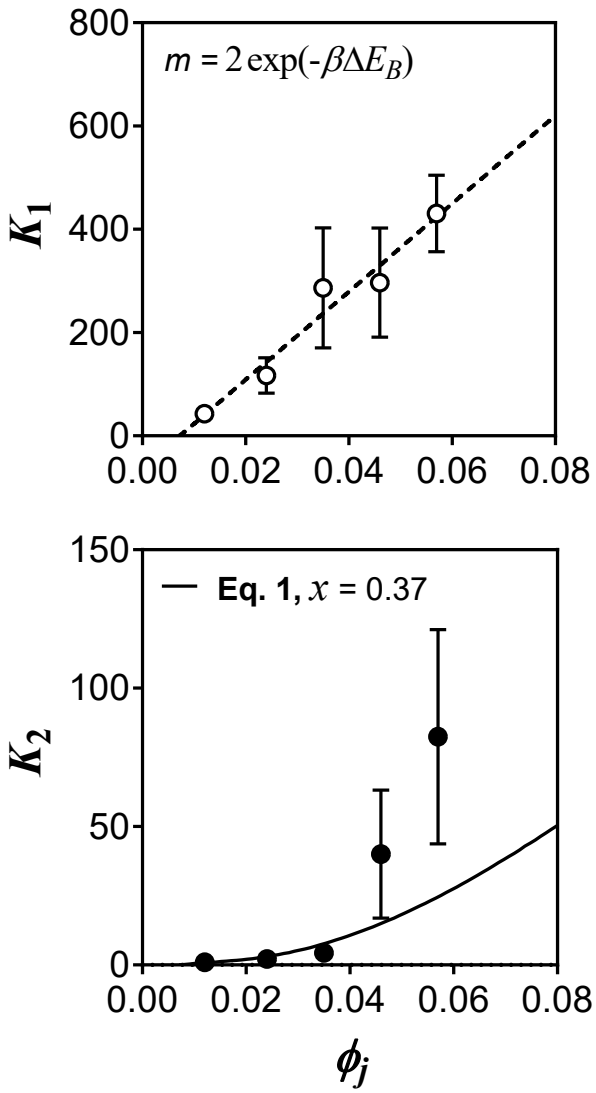

Supplementary Figure 2.14. Dependence of K_1 and K_2 on junction density in a 6-mesh network. The top panel shows a linear regression to the K_1 data, which provides an estimate for the network binding energy $\Delta E_B = -4.94$ kcal mol^{-1}. K_2 was estimated from this regression curve using **Eq. 1**, x = 0.37, and the experimental 6-mesh data (**Supplementary Tables 2.4** and **2.5**). Data points represent mean ± std. deviation for a total of n = 76 measurements, with ≥ 2 measurements per probe per concentration.

2.8 References

1. C. A. J. Hoeve, P. J. Flory, The Elastic Properties of Elastin. *J. Am. Chem. Soc.* **80**, 6523-6526 (1958).

2. H. G. Schild, D. A. Tirrell, Microcalorimetric Detection of Lower Critical Solution Temperatures in Aqueous Polymer-Solutions. *J Phys Chem-Us* **94**, 4352-4356 (1990).

3. D. E. Meyer, A. Chilkoti, Quantification of the effects of chain length and concentration on the thermal behavior of elastin-like polypeptides. *Biomacromolecules* **5**, 846-851 (2004).

4. S. M. Law, J. K. Gagnon, A. K. Mapp, C. L. Brooks, 3rd, Prepaying the entropic cost for allosteric regulation in KIX. *Proc Natl Acad Sci U S A* **111**, 12067-12072 (2014).

5. K. P. Ravindranathan, E. Gallicchio, R. A. Friesner, A. E. McDermott, R. M. Levy, Conformational Equilibrium of Cytochrome P450 BM-3 Complexed with N-Palmitoylglycine: A Replica Exchange Molecular Dynamics Study. *J. Am. Chem. Soc.* **128**, 5786-5791 (2006).

6. I. F. Thorpe, C. L. Brooks, Molecular evolution of affinity and flexibility in the immune system. *Proc Natl Acad Sci USA* **104**, 8821-8826 (2007).

7. J. Zimmermann *et al.*, Antibody evolution constrains conformational heterogeneity by tailoring protein dynamics. *Proc Natl Acad Sci U S A* **103**, 13722-13727 (2006).

8. S.-R. Tzeng, C. G. Kalodimos, Protein activity regulation by conformational entropy. *Nature* **488**, 236-240 (2012).

9. I. V. Nesmelova *et al.*, Lactose Binding to Galectin-1 Modulates Structural Dynamics, Increases Conformational Entropy, and Occurs with Apparent Negative Cooperativity. *J Mol Biol* **397**, 1209-1230 (2010).

10. W. C. Yount, H. Juwarker, S. L. Craig, Orthogonal Control of Dissociation Dynamics Relative to Thermodynamics in a Main-Chain Reversible Polymer. *J. Am. Chem. Soc.* **125**, 15302-15303 (2003).

11. W. C. Yount, D. M. Loveless, S. L. Craig, Small-Molecule Dynamics and Mechanisms Underlying the Macroscopic Mechanical Properties of Coordinatively Cross-Linked Polymer Networks. *J. Am. Chem. Soc.* **127**, 14488-14496 (2005).

12. D. Xu, S. L. Craig, Scaling Laws in Supramolecular Polymer Networks. *Macromolecules* **44**, 5465-5472 (2011).

13. Q. Chen, G. J. Tudryn, R. H. Colby, Ionomer dynamics and the sticky Rouse model. *J Rheol* **57**, 1441-1462 (2013).

14. T. Annable, R. Buscall, R. Ettelaie, D. Whittlestone, The Rheology of Solutions of Associating Polymers - Comparison of Experimental Behavior with Transient Network Theory. *J Rheol* **37**, 695-726 (1993).

15. S. C. Grindy *et al.*, Control of hierarchical polymer mechanics with bioinspired metal-coordination dynamics. *Nat Mater* **14**, 1210-1216 (2015).

16. W. A. Petka, J. L. Harden, K. P. McGrath, D. Wirtz, D. A. Tirrell, Reversible hydrogels from self-assembling artificial proteins. *Science* **281**, 389-392 (1998).

17. B. D. Olsen, J. A. Kornfield, D. A. Tirrell, Yielding Behavior in Injectable Hydrogels from Telechelic Proteins. *Macromolecules* **43**, 9094-9099 (2010).

18. D. D. McKinnon, D. W. Domaille, J. N. Cha, K. S. Anseth, Biophysically defined and cytocompatible covalently adaptable networks as viscoelastic 3D cell culture systems. *Adv Mater* **26**, 865-872 (2014).

19. F. Herbst, S. Seiffert, W. H. Binder, Dynamic supramolecular poly(isobutylene)s for self-healing materials. *Polym Chem* **3**, 3084-3092 (2012).

20. S. Tang, A. Habicht, S. Li, S. Seiffert, B. D. Olsen, Self-Diffusion of Associating Star-Shaped Polymers. *Macromolecules*, (2016).

21. P. B. Rapp *et al.*, Analysis and Control of Chain Mobility in Protein Hydrogels. *J. Am. Chem. Soc.*, (2017).

22. A. N. Semenov, M. Rubinstein, Thermoreversible Gelation in Solutions of Associative Polymers. 1. Statics. *Macromolecules* **31**, 1373-1385 (1998).

23. L. G. Baxandall, Dynamics of reversibly crosslinked chains. *Macromolecules* **22**, 1982-1988 (1989).

24. M. Rubinstein, A. N. Semenov, Thermoreversible Gelation in Solutions of Associating Polymers. 2. Linear Dynamics. *Macromolecules* **31**, 1386-1397 (1998).

25. M. Rubinstein, R. H. Colby, *Polymer Physics*. (Oxford University Press, 2003).

26. D. M. Soumpasis, Theoretical-Analysis of Fluorescence Photobleaching Recovery Experiments. *Biophys J* **41**, 95-97 (1983).

27. B. L. Sprague, R. L. Pego, D. A. Stavreva, J. G. McNally, Analysis of binding reactions by fluorescence recovery after photobleaching. *Biophys J* **86**, 3473-3495 (2004).

28. L. C. DeBolt, J. E. Mark, Theoretical study of the thermoelastic properties of elastin model chains. *Polymer* **28**, 416-422 (1987).

29. S. Fluegel, K. Fischer, J. R. McDaniel, A. Chilkoti, M. Schmidt, Chain Stiffness of Elastin-Like Polypeptides. *Biomacromolecules* **11**, 3216-3218 (2010).

30. W. Hassouneh, E. B. Zhulina, A. Chilkoti, M. Rubinstein, Elastin-like Polypeptide Diblock Copolymers Self-Assemble into Weak Micelles. *Macromolecules* **48**, 4183-4195 (2015).

31. L. Mandelkern, W. L. Mattice, Unperturbed dimensions of sequential copolypeptides containing glycine, L-alanine, L-proline, and γ-hydroxy-L-proline. *Biochemistry* **10**, 1934-1942 (1971).

32. W. G. Miller, C. V. Goebel, Dimensions of protein random coils. *Biochemistry* **7**, 3925-3935 (1968).

33. S. C. Tang, M. Z. Wang, B. D. Olsen, Anomalous Self-Diffusion and Sticky Rouse Dynamics in Associative Protein Hydrogels. *J. Am. Chem. Soc.* **137**, 3946-3957 (2015).

34. Y. Harpaz, M. Gerstein, C. Chothia, Volume changes on protein folding. *Structure* **2**, 641-649 (1994).

35. V. N. Malashkevich, R. A. Kammerer, V. P. Efimov, T. Schulthess, J. Engel, The crystal structure of a five-stranded coiled coil in COMP: A prototype ion channel? *Science* **274**, 761-765 (1996).